Dynamic Finite Element and Experimental Strain Analysis of a Passenger Car Rear Axle for Durable and Sustainable Suspension Design

Ionut Daniel Geonea *, Ilie Dumitru, Laurentiu Racila, Cristian Copilusi

Posted Date: 19 December 2025

doi: 10.20944/preprints202512.0984.v1

Keywords: rear axle; durability test bench; flexible multibody dynamics; explicit dynamic finite element analysis; strain-gauge measurements; response-surface optimisation; wheel spindle design

 doi:10.20944/preprints202512.0984.v1

Article

Dynamic Finite Element and Experimental Strain Analysis of a Passenger Car Rear Axle for Durable and Sustainable Suspension Design

Ionut Daniel Geonea [1,*], Ilie Dumitru [2], Laurentiu Racila[2] and Cristian Copilusi [1]

[1] University of Craiova, Faculty of Mechanics, Department of Applied Mechanics and Civil Engineering, Craiova Romania

[2] University of Craiova, Faculty of Mechanics, Department of Automotive, Transportation and Industrial Engineering, Craiova Romania

* Correspondence: ionut.geonea@edu.ucv.ro

Abstract

This paper proposes an integrated numerical–experimental methodology for the durability assessment and optimisation of a passenger-car rear axle. A dedicated rear-suspension durability test bench was designed to impose a controlled cyclic vertical excitation on a dependent axle, reproducing service-like translational and rotational amplitudes of the beam and stabilizer bar. A detailed flexible multibody model of the bench–axle system was developed in MSC ADAMS and used to tune the kinematic excitation and determine an equivalent design load at the wheel spindles, consistent with the stiffness of the suspension assembly. Experimental strain measurements at nine locations on the axle, acquired with strain-gauge instrumentation on the bench, were converted into stresses and used to validate an explicit dynamic finite element model in ANSYS. The FE predictions agree with the experiments within about 10% at the beam mid-span and correctly identify a critical region at the junction between the side plate and the arm, where peak von Mises stresses of about 104 MPa occur. The validated model then supports a response-surface-based optimisation of the safety-critical wheel spindle, yielding a geometry that lowers spindle-fillet stresses to around 180–185 MPa under the maximum admissible wheel load, with only a modest mass penalty.

Keywords: rear axle; durability test bench; flexible multibody dynamics; explicit dynamic finite element analysis; strain-gauge measurements; response-surface optimisation; wheel spindle design

1. Introduction

The current state of research on the design, optimization and testing of suspension components and rear axle assemblies in road vehicles shows a clear trend towards combining advanced numerical modeling with dedicated test rigs, as well as towards the use of modern multi-objective optimization methods. A critical synthesis of optimization methods used in road vehicle design – including deterministic algorithms, metaheuristics, response-surface-based techniques and multicriteria formulations – is provided by Gobbi et al. [1], who emphasize the need to couple vehicle dynamic models with structural, comfort and safety criteria. In the same direction, Yıldız et al. propose a metaheuristic equilibrium optimization algorithm coupled with a response-surface-based metamodel for the structural optimization of vehicle components [2], demonstrating the potential of such approaches to reduce mass and computational cost while still satisfying strength constraints.

1.1. Structural and Fatigue Optimization of Chassis and Axle Components

A significant part of the literature focuses on geometric and structural optimization of components in the rear axle and chassis area, closely linked to fatigue phenomena and failures

 doi:10.20944/preprints202512.0984.v1

observed during development testing. Kumar and Kumaraswamidhas analyze the causes of failures occurring during developmental testing of a fabricated rear axle housing, and propose a geometry optimization procedure aimed at eliminating stress concentrations identified by finite element analysis and increasing the durability of the assembly [3]. For heavy-duty vehicles, Zheng et al. apply both topology optimization and multi-objective optimization to a drive axle housing, seeking to reduce mass, increase stiffness and improve fatigue performance, based on advanced FEM models and iterative–evolutionary procedures [4].

At the level of connection subassemblies, Topaç et al. demonstrate, on a rear axle connection bracket for heavy commercial vehicles, that topology optimization can lead to significant mass reduction without penalizing stress levels and overall stiffness [5]. Park et al. use a Design of Experiments (DoE) approach to optimize several rear chassis components, combining FEM analysis with experimental design techniques to identify lightweight design variants that satisfy strength and natural frequency constraints [6].

Failure mode analysis and design improvement of severely loaded subassemblies is also addressed in the work of Topaç et al. on an eccentrically loaded connecting rod in a double front axle steering linkage prototype [7]. The authors combine stress analysis with fatigue assessment for different design variants, identifying geometric modifications that yield a more favorable stress distribution and increased service life. Jeong et al. focus on the shape optimization of a torsion beam axle, correlating its geometric parameters with the handling performance of the vehicle and using an optimization procedure that improves directional response while satisfying structural constraints [8].

In the field of safety components and steering elements, Balta et al. apply Pareto optimization to the design of a heavy truck rear underrun protection system, simultaneously considering regulatory load cases and the mass of the structure [9]. Senniappan et al. address the optimization of a steering tie rod arm for a commercial vehicle based on a strain-life fatigue criterion, calibrated by experimental testing and FEM analysis, in order to obtain a configuration robust against cyclic loading [10].

Adopting a system-level perspective, Zhou et al. propose a cooperative multi-objective optimization algorithm for the design of a vehicle axle system, where objectives such as mass, stiffness and reliability are considered simultaneously [11]. With regard to torsional vibration, Hao et al. develop a coupled driveline–rear axle model and perform uncertainty analysis and parameter optimization in order to limit driveline torsional vibration amplitudes [12]. Taken together, these studies show that modern rear axle and associated component design increasingly relies on the combination of detailed FEM models, fatigue assessment and advanced multi-objective optimization techniques, often supported by metamodeling and evolutionary algorithms [1–3,4–6,8–12].

1.2. Test Benches for Suspension, Axles and Elastic Components

Complementary to numerical optimization, a major research direction is the development of test benches for experimental validation of suspensions, elastic elements and axle assemblies. Early contributions focus on dedicated rigs for leaf springs and suspensions of commercial vehicles. Soares et al. describe a test bench for static and dynamic tests of suspension leaf springs, capable of reproducing conditions close to real operation and providing data for numerical model calibration [13]. A subsequent work by the same group presents a multiaxial bench for testing the suspension of commercial vehicles, which enables the simultaneous application of vertical, longitudinal and lateral loads and highlights the advantages of bench testing compared to full-vehicle tests [14].

For suspension parameter identification and testing, quarter-car rigs form a distinct category. Mitra et al. use a quarter-car test rig to apply DoE methods to suspension optimization, analyzing the influence of key parameters on the dynamic response [15]. In a related paper, the same authors propose a derivative-free, DoE-based optimization method for automotive suspension systems, which makes it suitable for nonlinear problems or computationally expensive numerical models [16]. Salah proposes the design, implementation and integration of a laboratory-scale automotive suspension test rig, intended for both research and teaching activities, where different control strategies and design configurations can be evaluated [17]. Alzughaibi et al. address the modeling of

 doi:10.20944/preprints202512.0984.v1

a passive suspension test rig, highlighting the role of nonlinear friction forces in system dynamics and the need for more sophisticated models for parameter identification [18]. Recent developments target the full automation of quarter-car test benches, including actuator control, data acquisition and processing, which increases repeatability and efficiency in testing campaigns [19].

There are also test benches focused on specific operating regimes. Liao et al. propose the design, modeling and verification of a test bench for braking simulation of a quarter vehicle, combining dynamic modeling with experimental tests for calibration [20]. From the standpoint of vibration isolation and the interaction between the bench and its foundation, Croce et al. analyze design criteria for automotive test benches and propose isolation solutions that reduce the transmission of vibrations to surrounding structures and improve measurement quality [21].

Beyond suspension and spring benches, Favilli et al. propose an innovative tire–road test bench capable of using real asphalt surfaces and reproducing modern operating conditions (high speeds, varying contact conditions), which allows integrated assessment of tire performance and, indirectly, of associated chassis elements [22]. These developments illustrate a trend from mono-axial or simplified test benches towards multiaxial rigs with advanced control and instrumentation capabilities, intended to reproduce real driving conditions as closely as possible [13–15,16–20].

1.3. Test Benches and Virtual Concepts for Powertrain and Steering–Suspension Systems

In parallel with suspension and axle testing, the literature also addresses test benches for powertrains and integrated vehicle systems. Mántaras and Luque introduce the concept of a "virtual test rig" for steering and suspension systems, based on multibody modeling, which enables the evaluation and optimization of geometric and elastokinematic parameters prior to physical prototyping, thus reducing development time and cost [23]. In the field of electric powertrains, El Hadraoui et al. propose a customizable test bench for an electric vehicle powertrain, developed using a Model-Based Systems Engineering (MBSE) methodology, with emphasis on flexibility, modularity and use for educational and research purposes [24].

Andert et al. present the "virtual shaft" concept, a synchronized motion control strategy for real-time testing of automotive powertrains, in which real and virtual components are coupled in a hardware-in-the-loop configuration, allowing faithful reproduction of operating conditions and dynamic interactions in the driveline [25]. These approaches show that the development of modern test benches tends to be integrated with real-time modeling and closed-loop coupling with numerical models, going beyond the paradigm of purely experimental rigs.

1.4. Integration of Optimization Methods with Bench Testing – Implications for the Rear Axle

Overall, the reviewed literature indicates two major directions that are still insufficiently integrated: on the one hand, structural and fatigue optimization of rear-axle-related components based on FEM, fatigue assessment and multi-objective optimization [1–3,4–12], and, on the other hand, the development of test benches for suspensions, springs and chassis subassemblies, including automated quarter-car rigs and multiaxial benches for commercial vehicles [13–15,16–20]. Although some studies employ experimental methods for calibrating numerical models or for partial validation of optimized solutions, relatively few works propose a fully integrated methodology combining multibody modeling for load generation, detailed FEM analysis of a real rear axle, dedicated test benches for rear suspension testing and explicit durability assessment under representative operating conditions.

Furthermore, most of the analyzed test benches are either oriented toward simplified suspension representations (quarter-car), elastic components (leaf springs), or powertrain subsystems, without explicitly targeting a passenger car rear axle as the central object of evaluation. In the current context, characterized by stringent mass reduction requirements, increased durability demands and the need to adapt to electrified vehicles (with different masses and load distributions), there is a clear need for an integrated methodology and a dedicated test bench that enable rear axle durability testing directly correlated with advanced numerical modeling and modern structural optimization procedures. This

 doi:10.20944/preprints202512.0984.v1

intersection between test bench development, multibody modeling, FEM analysis and multi-objective optimization defines the gap that the proposed work aims to address.

2. Experimental Test Bench for Rear Suspension Durability Testing

This section presents the dedicated test bench developed for the durability assessment of a passenger car rear suspension. The rig has been conceived to reproduce, in a controlled and repeatable manner, the cyclic loading acting on a dependent rear axle and its associated elastic elements, while allowing direct comparison between numerical predictions and experimental measurements of stresses and strains.

2.1. Concept and Kinematic Layout

The test bench is designed to excite the rear suspension through a crank–rocker mechanism that converts the rotary motion of an electric drive into a nearly harmonic vertical motion at the wheel spindle. The kinematic chain consists of a crank mounted on the motor shaft, an adjustable-length connecting rod and a rocker arm pivoted to the bench frame. The distal end of the rocker is connected to the rear axle assembly through a bushing, so that the imposed motion generates a cyclic vertical force on one wheel side of the axle.

The rear axle, complete with helical coil springs and stabilizer bar, is installed on the rig using mounting conditions that reproduce as closely as possible the actual interfaces on the vehicle body. The bench frame provides rigid supports for the axle trailing arms and spring seats, while the crank–rod–rocker mechanism excites the right wheel side. This arrangement enables the investigation of both global bending of the axle beam and local stress concentrations in critical regions, under a loading pattern representative of service conditions.

The stroke of the rocker and the amplitude of the imposed load can be adjusted by modifying the effective length of the connecting rod and the crank radius. In this way, the same bench can be used to test different rear axle geometries and to reproduce various severity levels of service loading.

2.2. CAD Model and Virtual Prototyping

A detailed three-dimensional model of the test bench and rear suspension has been created in SolidWorks. The CAD assembly includes the bench frame, crank–rod–rocker drive mechanism, bushings, rear axle beam, helical coil springs, stabilizer bar and the auxiliary fixtures required for mounting the axle on the rig.

The CAD model serves a dual purpose. First, it provides the geometric basis for manufacturing the bench components and for verifying assembly clearances and ranges of motion. Second, it is used as input for the multibody dynamic model developed in MSC ADAMS, in which the crank–rod–rocker mechanism and the rear axle are represented as a system of rigid and flexible bodies connected by kinematic joints and compliant elements.

Within the ADAMS environment, the stabilizer bar and the rear axle beam are modeled as deformable solids, allowing the computation of displacements, deformations and internal forces in these components under cyclic excitation. The simulation results are subsequently used to define the load cases for the finite element analysis and to support the design of the experimental test programme.

The kinematic scheme of the test bench is shown in Figure 1a, while the corresponding 3D CAD model developed in SolidWorks is presented in Figure 1b. In the kinematic sketch, the rear axle assembly is represented in its test position between the vertical uprights of the bench. The lower oscillating beam (3) acts as a rocker that transforms the input motion into a vertical displacement of the right wheel side. The excitation is introduced with a prescribed eccentricity e indicated by item (1), so that the imposed rotation of the rocker generates an alternating vertical motion at its ends.

This motion is transmitted through link 2 (item 2) and the vertical links (4) and (4′) to the axle and to the coil springs (6), reproducing the relative vertical displacement between the axle and the

 doi:10.20944/preprints202512.0984.v1

vehicle body. Link 4 provides the mechanical connection between the rocker beam (3) and the right side of the axle, and therefore concentrates the main load path from the drive mechanism to the axle assembly.

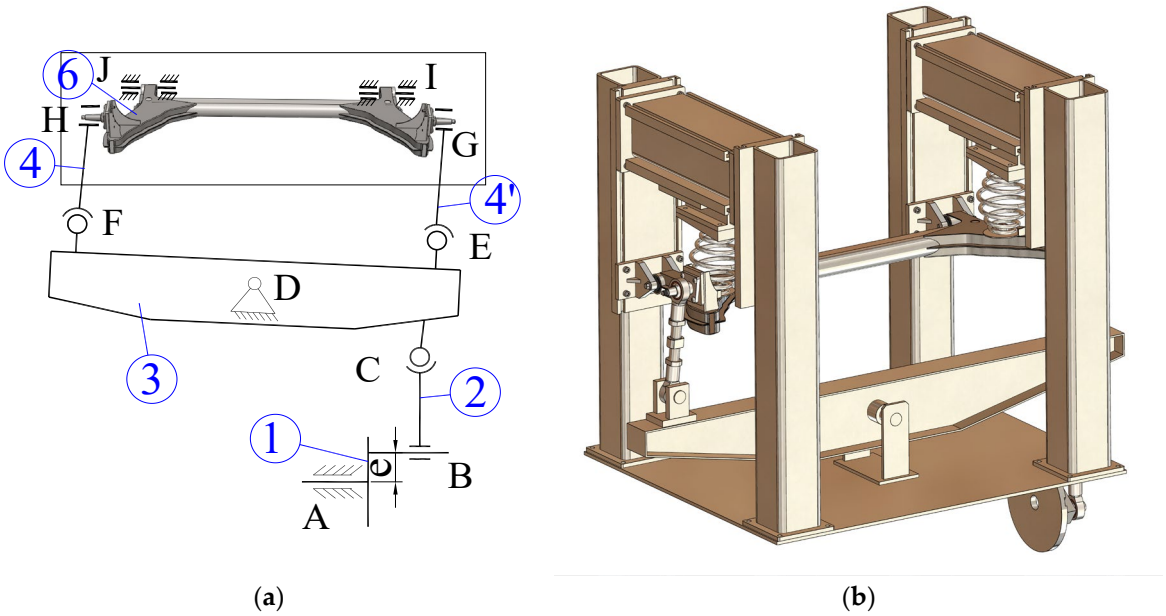

(**a**) (**b**)

Figure 1. Kinematic scheme and CAD model of the rear suspension durability test bench: (**a**) kinematic scheme of the excitation mechanism and rear axle assembly (1—eccentricity e; 2—connecting link; 3—rocker beam; 4, 4′—vertical links; 6—rear axle with coil springs); (**b**) SolidWorks model of the test bench.

The SolidWorks model (Figure 1b) details the actual geometry of the test bench built according to this kinematic scheme. The structure consists of a base frame and two stiff vertical portals, assembled from rectangular profiles using threaded joints and bolted connections, rather than welded joints. The dependent rear axle is mounted between the portals, with its trailing arms clamped to brackets on the frame and the helical coil springs installed between the axle seats and the adjustable upper supports attached to the uprights. The lower rocker beam is pivoted to the base frame at its centre and connected to the axle on the right-hand side via link 2 and the vertical linkage, in accordance with the schematic in Figure 1a.

The 3D model includes all functional components of the bench—frame, rocker, links, spring seats, guides and fastening elements—and has been used both to check assembly clearances and to export geometry to the multibody and finite element models employed in the subsequent numerical analysis.

2.3. Mounting of the Rear Axle Assembly on the Bench

The dependent rear axle considered in this study consists of a central beam, two trailing arms made of bent sheet metal, end plates, spring seats and brackets for the stabilizer bar. In the vehicle, the axle is connected to the body through flexible bushings and supported by helical coil springs.

On the test bench, the axle is mounted in a configuration that reproduces the kinematic boundary conditions of the vehicle installation. The trailing arms are clamped to rigid supports that mimic the body brackets, and the coil springs are mounted between the axle seats and fixed upper seats attached to the frame. The stabilizer bar is installed in its operational position, with its ends connected to the axle through links and bushings.

The right wheel spindle location is connected to the rocker arm via a bushing and a short link. The excitation force is thus transmitted directly to the spindle region, generating bending of the axle beam and relative motion in the suspension joints similar to those encountered in service. By acting

 doi:10.20944/preprints202512.0984.v1

on booth's wheels side, a symmetric loading condition is created, which is particularly demanding for the beam and the welded joints near the wheel spindles.

2.4. Loading System and Test Conditions

The stand is driven by an electric motor operating at a constant speed, which imposes a cyclic motion of the crank and, consequently, of the rocker arm. For the present study, the operating parameters of the rig have been selected such that the maximum dynamic force transmitted to the right wheel spindle reaches approximately 15,000 N, in line with the values obtained from the multibody simulations for severe road excitation.

The resulting operating cycle consists of repeated load reversals over a given number of cycles, corresponding to an accelerated durability test. After a short run-in period, the system reaches a steady-state regime in which the force in the connecting rod and the stresses in the axle structure exhibit nearly periodic behaviour. This regime is used for both numerical–experimental correlation and fatigue-related assessment.

The test bench is designed to allow variation of the excitation frequency, stroke and mean position of the rocker arm, so that different duty cycles can be imposed on the same axle configuration. This flexibility is essential for studying the influence of loading severity and spectrum on the stress distribution and on the anticipated fatigue life of the axle.

3. Dynamic Simulation of the Test Bench in ADAMS

The kinematic scheme and CAD model presented in Section 2 were used as a basis to build a detailed multibody model of the test bench in MSC ADAMS. The objective of this model is twofold: (i) to evaluate the kinematic amplitudes and dynamic loads transmitted to the rear axle and stabilizer bar during fatigue testing, and (ii) to provide design loads for the subsequent finite element analysis of the rear axle assembly.

3.1. Multibody Modelling Strategy

The CAD assembly created in SolidWorks was exported in Parasolid format and imported into ADAMS/View. The rigid parts of the stand (base frame and vertical uprights) were merged into a single body and fixed to ground. The driving mechanism is modelled as a planar four-bar linkage, consistent with the kinematic scheme in Figure 1a:

In the kinematic scheme of the test bench (Figure 1a), the kinematic pairs are labelled A–J and are defined as follows:

- Joint A – revolute joint between the fixed frame (ground) and the crank (link 1), corresponding to the motor shaft.
- Joint B – revolute joint between the crank (link 1) and the adjustable connecting link (link 2).
- Joint C – spherical joint between the connecting link (link 2) and the rocker beam (link 3), which accommodates the relative angular misalignment between the two members.
- Joint D – revolute joint between the rocker beam (link 3) and the fixed frame.
- Joints E and F – spherical joints between the rocker beam (link 3) and the vertical connecting links (links 4′ and 4, respectively), allowing the links to follow the motion of the axle without overconstraining the mechanism.
- Joints G and H – cylindrical (revolute) joints between the upper ends of the vertical connecting links (4′ and 4) and the wheel-spindle regions of the rear axle (link 6), transmitting the vertical load from the mechanism to the axle while allowing rotation about the spindle axis.
- Joints I and J – cylindrical (revolute) joints between the rear axle (link 6) and the test-bench frame. These joints represent the bushings through which the axle is guided relative to the uprights of the stand and ensure that the axle is constrained to move according to the bench kinematics. The helical coil springs are modelled separately as spring–damper force elements acting between

 doi:10.20944/preprints202512.0984.v1

markers on the axle, located in the vicinity of joints I and J, and corresponding markers on the upper supports of the frame.

This explicit definition of the kinematic pairs A–J is used consistently in the ADAMS model, ensuring a one-to-one correspondence between the schematic representation in Figure 1a and the multibody model.

- Link 1 – Crank: the eccentric crank driven by the electric motor. Link 1 is connected to the fixed frame via a revolute joint whose axis is normal to the motion plane.
- Link 2 – Adjustable connecting link: the threaded link that transmits motion from the crank to the rocker beam. Its effective length can be modified in the CAD and in the multibody model to reproduce different stroke amplitudes. In ADAMS, link 2 is connected to the crank (link 1) by a revolute joint and to the rocker beam (link 3) by a spherical joint, allowing for the small angular misalignments that occur during motion.
- Link 3 – Rocker beam: the lower beam that oscillates about a fixed pivot on the stand frame. A revolute joint connects link 3 to the frame, while a spherical joint connects it to the adjustable connecting link (link 2). The geometry of the rocker beam is identical to the CAD model, so that the points of attachment of the vertical connecting links (4 and 4′) are preserved.
- Links 4 and 4′ – Vertical connecting links: rigid links that transmit the motion of the rocker beam to the rear axle. Each link is connected to the rocker beam (link 3) by a spherical joint and to the corresponding wheel spindle region of the axle by a cylindrical (revolute) joint, thus allowing the necessary relative rotations between the parts while carrying the vertical load.
- Link 6 – Rear axle assembly with stabilizer bar: the complete rear axle beam with its brackets and the stabilizer bar are imported from CAD as a single body in the initial model and later replaced by flexible bodies (Section 3.2).

The crank is prescribed a periodic rotational motion about its axis. In the simulations reported here a harmonic law is used, with angular position $\phi(t)=\phi_0+\Delta\phi\sin(2\pi ft)$, where ϕ_0 is the mean angle, $\Delta\phi$ the amplitude and f the test frequency. These parameters are selected such that the vertical displacement at the wheel spindle reproduces the target fatigue loading conditions of the rear axle. Gravity acts along the global negative Z-direction; the global X-axis is aligned with the longitudinal direction of the axle beam.

Contact between the stand and the floor is neglected, because the base frame is bolted to the foundation in the real installation and its motion is negligible. The clearance in revolute joints is also neglected; joints are assumed ideal without friction. This leads to a conservative estimate of the internal forces in the rear axle and stabilizer bar.

3.2. Flexible Representation of the Rear Axle and Stabilizer Bar

To correctly evaluate stress-related quantities and local deformations, the rear axle beam and stabilizer bar cannot be treated as perfectly rigid. Therefore, these components are introduced as flexible bodies using the dedicated functionality available in ADAMS (Figure 2).

A finite element model of the rear axle–stabilizer-bar assembly is first generated starting from the CAD geometry and the nominal material properties of the steel. The mesh combines shell and solid elements in the regions with complex geometry (such as the bent side plates and welded brackets). This FE model is then reduced to a modal neutral file (MNF), retaining the lowest natural modes that are relevant for the operating frequency range of the stand. The MNF is imported into ADAMS/Flex and replaces the corresponding rigid body. The locations of all joints, bushings and load application points are mapped to interface nodes of the flexible body.

A reference marker is placed at the centre of mass of the stabilizer bar. The translational displacements and elastic deformations of this point along the global X- and Y-axes are later used both for evaluating the dynamic behaviour of the stand and for comparison with experimental measurements.

 doi:10.20944/preprints202512.0984.v1

3.3. Simulation Scenarios and Post-Processing

Dynamic simulations are performed in the time domain for a sequence of crank revolutions, starting from rest. An initial transient interval is discarded so that the analysis focuses on the steady-state response under periodic loading. The integration is carried out with a variable-step algorithm with error control adequate for flexible multibody systems; the maximum step size is limited in order to capture the higher-frequency modes of the axle–stabilizer assembly.

In all simulations, the crank at joint A is driven with a constant angular velocity of ω=15.5 rad/s (corresponding to an excitation frequency of approximately 2.47 Hz), matching the operating speed used in the experimental tests.

The main output quantities used in the subsequent analysis are:

- translational displacements, velocities and accelerations of the marker at the stabilizer bar centre of mass along the global X- and Y-directions;
- relative rotations of the stabilizer bar about its longitudinal axis, which correlate with the torsional deformation of the bar;
- reaction forces in the vertical connecting links (links 4 and 4′), transmitted through the spherical joint on the rocker beam and the cylindrical joint on the wheel spindle region, which indicate how the excitation is transmitted from the mechanism to the axle;
- internal forces at the wheel spindles, obtained by defining force sensors at the connection between the axle and the wheel-hub region.

Figure 2 illustrates the multibody model of the rear suspension durability test bench implemented in MSC ADAMS, highlighting both the overall assembly and, in particular, the vertical connecting link (4) with its spherical joint E to the rocker beam and cylindrical joint G to the wheel-spindle region of the rear axle.

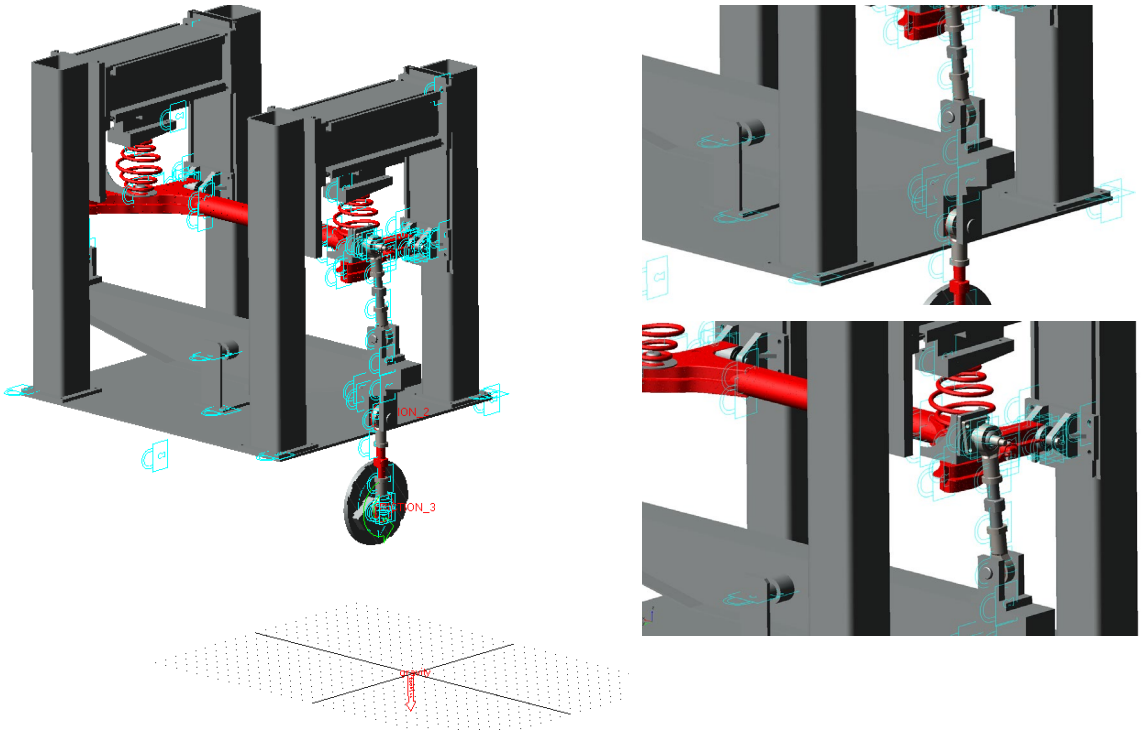

(**a**) (**b**)

Figure 2. Multibody model of the rear suspension durability test bench in MSC ADAMS: (**a**) overall dynamic model including the flexible rear axle, stabilizer bar, springs and driving mechanism; (**b**) detail of the vertical connecting link (4) showing the spherical joint E to the rocker beam and the cylindrical joint G to the wheel-spindle region of the axle.

 doi:10.20944/preprints202512.0984.v1

The multibody simulation also provides the reaction forces in joint E, which represents the main load path through which the excitation of the mechanism is transmitted to the right side of the rear axle. Figure 3 shows the time histories of the force components F_X, F_Y and F_Z in this joint (Joint 86 in ADAMS). It can be observed that the dominant component is the vertical force F_Z, whereas the longitudinal and lateral components F_X and F_Y remain comparatively small, confirming that the stand primarily excites the axle in vertical bending with only minor parasitic loads in the other directions.

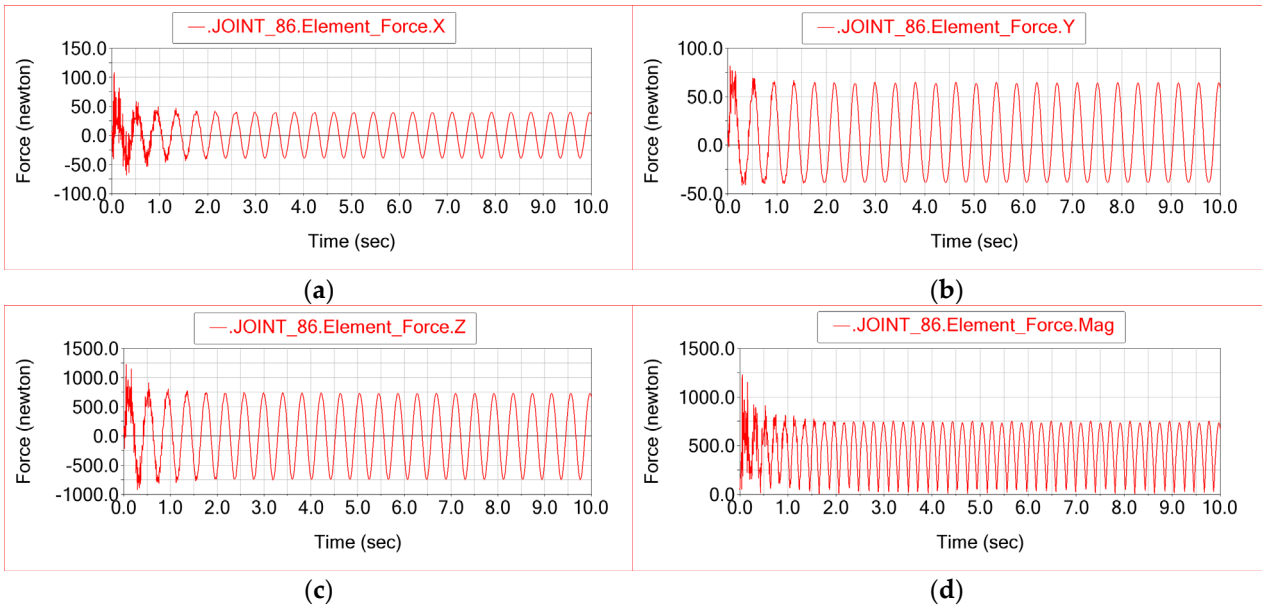

Figure 3. Time histories of the reaction force components F_X, F_Y and F_Z in joint E (Joint 86 in ADAMS), corresponding to the cylindrical connection between the vertical connecting link (4′) and the right wheel-spindle region of the rear axle: (**a**) F_X, (**b**) F_Y,(**c**) F_Z and (**d**) Magnitude Force.

In addition to joint E, the reaction forces were evaluated in joint G, which represents the cylindrical connection between the upper end of the vertical connecting link (4′) and the right wheel-spindle region of the rear axle. Figure 4 shows the time histories of the three force components F_X, F_Y and F_Z in this joint (Joint 95 in ADAMS), while panel (d) presents the magnitude of the reaction force $|F|$. After a short transient in the first second of simulation, the response becomes strictly periodic. The dominant contribution is given by the F_Z component, which reaches peak values close to±800±1000 N, whereas the F_X and F_Y components remain below about ±60–±70 N. This confirms that the connection between link 4′ and the wheel spindle is loaded predominantly in the direction that is approximately aligned with the vertical motion imposed by the test bench, while the longitudinal and lateral force components are comparatively small.

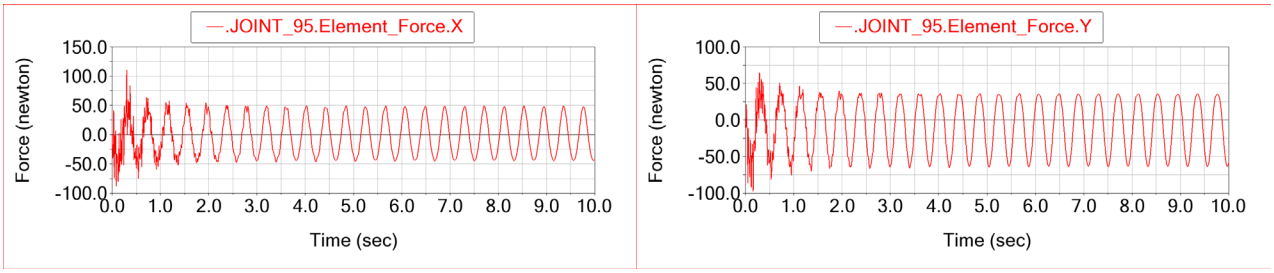

 doi:10.20944/preprints202512.0984.v1

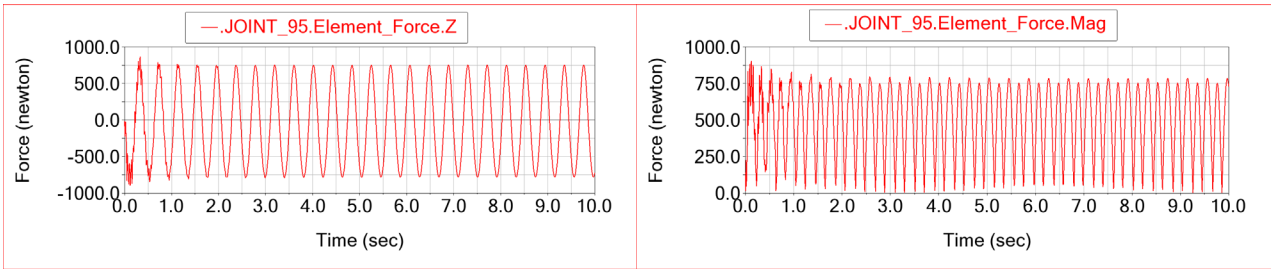

(**c**) (**d**)

Figure 4. Time histories of the reaction force components at joint G (Joint 95 in ADAMS) between the vertical connecting link (4′) and the right wheel-spindle region of the rear axle: (**a**) F_X, (**b**) F_Y, (**c**) F_Z, and (d) magnitude of the reaction force.

Besides the reaction forces in the kinematic joints, the dynamic simulation provides the translational displacements, velocities and accelerations of any marker in the model, as well as the corresponding elastic deformations of the flexible rear stabilizer bar.

In order to characterise the global motion of the rear stabilizer bar during the test cycle, the translational displacements of its centre of mass were monitored in the ADAMS model. Figure 5 shows the time histories of the three Cartesian components and of the displacement magnitude. After the initial transient, the response becomes clearly periodic, with small-amplitude oscillations of the order of a few millimetres. The longitudinal displacement component remains very small compared with the other two components, indicating that the stabilizer bar is mainly subjected to vertical and lateral motion, consistently with the intended loading mode of the test bench.

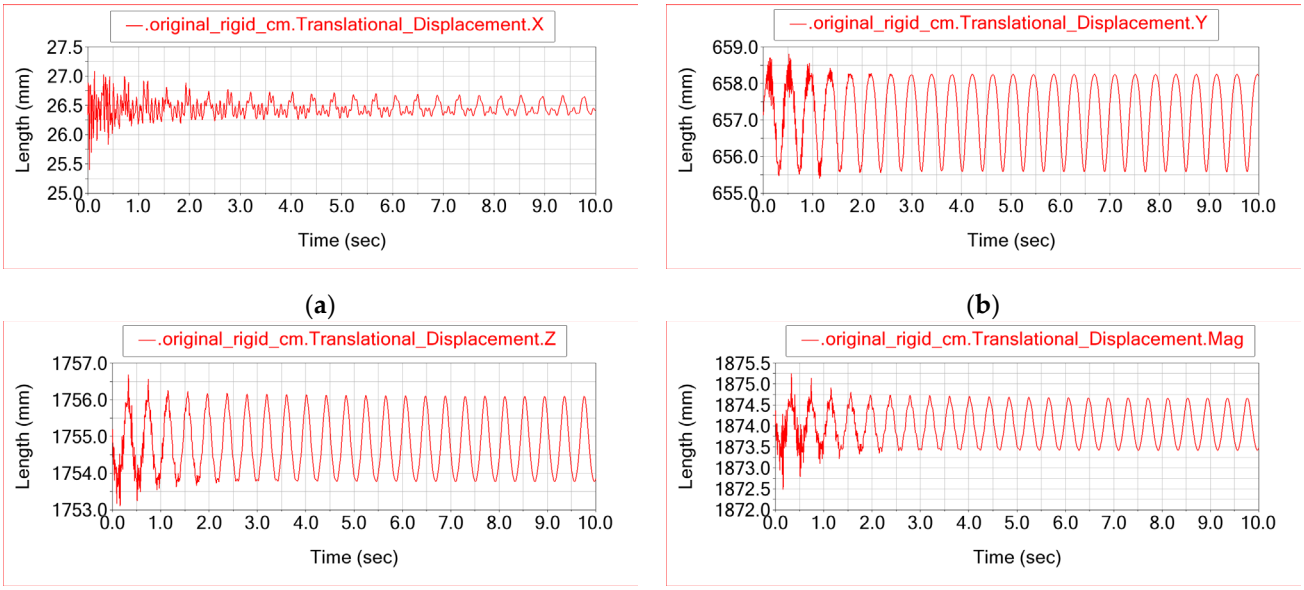

(**a**) (**b**)

(**c**) (**d**)

Figure 5. Time histories of the translational displacements of the centre of mass of the rear stabilizer bar in the global coordinate system: (a) displacement u_X; (b) displacement u_Y; (c) displacement u_Z; (d) magnitude of the displacement $|u|$.

To distinguish between rigid-body motion and elastic behaviour, the translational deformations of the centre-of-mass marker of the rear stabilizer bar with respect to its reference node were also monitored. Figure 6 shows the time histories of the three Cartesian components of this deformation and of its magnitude. After the initial transient, the response becomes purely periodic. The δ_X component remains almost negligible, while δ_Y and δ_Z reach amplitudes of the order of 1 mm, indicating that the stabilizer bar mainly deforms in the vertical and lateral directions under the imposed excitation.

 doi:10.20944/preprints202512.0984.v1

In the ADAMS/Flex model, the motion of the marker attached to the centre of mass of the stabilizer bar can be decomposed into a rigid-body contribution and an elastic contribution. The translational displacement outputs (Figure 5) represent the total motion of the marker in the global reference frame, i.e., the sum of the rigid-body motion of the bar and its local elastic deflection. By contrast, the translational deformation outputs (Figure 6) represent only the elastic part of the motion, measured with respect to the reference node of the flexible body. Consequently, the deformation amplitudes are much smaller than the corresponding displacements and directly reflect the bending and torsional flexibility of the stabilizer bar under the imposed excitation.

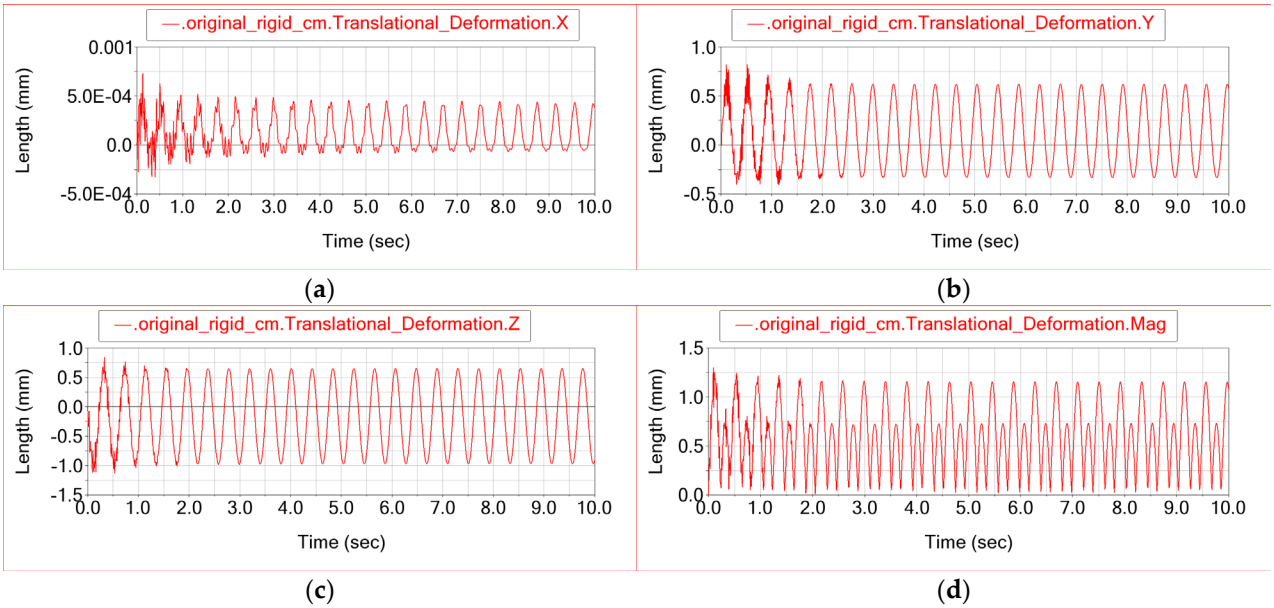

Figure 6. Time histories of the translational elastic deformations of the centre of mass of the rear stabilizer bar: (a) deformation δ_X; (b) deformation δ_Y; (c) deformation δ_Z; (d) magnitude of the deformation $|\delta|$.

In addition to the translational deformations, the ADAMS/Flex model provides the rotational elastic deformations of markers attached to the flexible stabilizer bar. Figure 7 shows the time histories of the rotational deformation components θ_X, θ_Y and θ_Z for a marker located in the vicinity of the bar's centre of mass, together with the magnitude of the rotation $|\theta|$. These quantities describe the local twist and bending rotations of the stabilizer bar relative to its reference configuration. After the initial transient, the response becomes periodic, with the dominant contribution associated with the rotation about the bar's longitudinal axis (X), confirming that the excitation applied by the test bench produces a significant torsional deformation of the stabilizer bar superimposed on its bending motion.

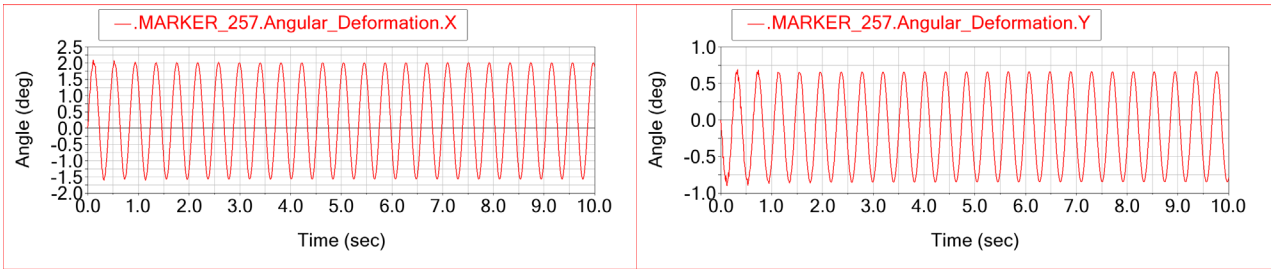

 doi:10.20944/preprints202512.0984.v1

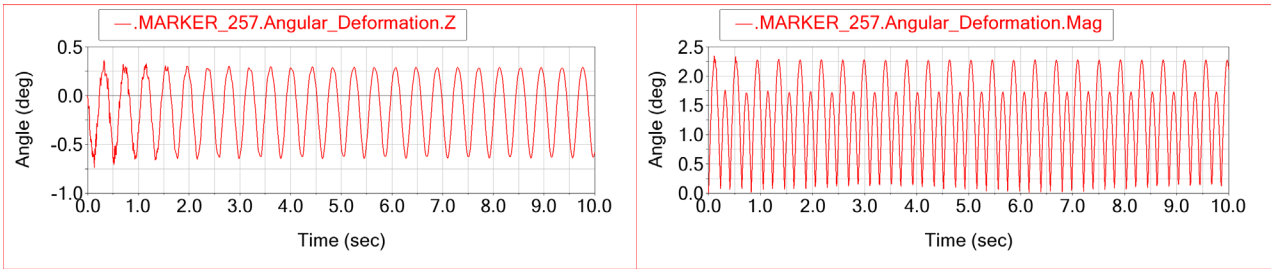

(**c**) (**d**)

Figure 7. Time histories of the rotational elastic deformations of a marker located near the centre of mass of the rear stabilizer bar: (a) θ_X; (b) θ_Y; (c) θ_Z; (d) magnitude of the rotation $|\theta|$.

The ADAMS/Flex model also enables a direct three-dimensional visualisation of the deformation of the flexible components. As illustrated in Figure 7, deformed shapes corresponding to different vibration modes or to selected instants of the transient response can be displayed for the rear stabilizer bar and the rear axle assembly. In addition, coloured contour plots of the deformation field and full 3D animations of the simulated motion have been generated; these are provided as supplementary video material to better illustrate the dynamic behaviour of the test bench and of the rear suspension components.

3.4. Discussion of Dynamic Response

The ADAMS model confirms that the test bench reproduces the intended loading mode of the rear axle. The crank at joint A, driven at a constant angular velocity of ω=15.5 rad/s, imposes a nearly harmonic motion on the rocker beam (link 3), which in turn drives the vertical connecting links (4 and 4′) through the spherical joints E and F. The loads are then transmitted to the rear axle through the cylindrical joints G and H, exciting the axle beam and the stabilizer bar in a combined bending–torsion mode. After a short transient, all relevant kinematic and kinetic quantities exhibit a purely periodic response. The time histories of displacement and deformation at the stabilizer-bar centre of mass are nearly sinusoidal, as expected from the harmonic drive, while small higher-frequency components are associated with the flexible modes of the axle assembly.

Besides the reaction forces in the joints, the dynamic simulation provides the translational displacements, velocities and accelerations of any marker in the model. Figures 5 and 6 illustrate, respectively, the total translational displacements and the translational elastic deformations of the marker located at the centre of mass of the rear stabilizer bar. The displacement histories in Figure 5 describe the global oscillatory motion imposed by the test bench, whereas the deformation histories in Figure 6 represent only the elastic part of this motion, relative to the reference node of the flexible body. The deformation amplitudes are significantly smaller than the corresponding displacements and are mainly associated with the lateral and vertical components, indicating that the stabilizer bar undergoes modest but clearly periodic bending and torsional deflection under the imposed excitation. The associated velocity and acceleration histories (not shown in paper) follow the same pattern, with smooth, nearly sinusoidal steady-state behaviour.

The reaction forces transmitted along the load path are quantified in joints E and G. Figures 3 and 4 show the time histories of the three Cartesian components and of the magnitude of the reaction force in these joints. After the initial transient, the resultant forces stabilise to nearly constant amplitudes and remain strongly dominated by a single component (here aligned with the global Z-direction), while the other two components are much smaller. This confirms that the mechanism primarily excites the rear axle in the intended loading direction, with only minor parasitic loads in the orthogonal directions, and that no undesirable kinematic amplification or spurious constraints are introduced by the joint configuration.

In addition, the flexible multibody model allows three-dimensional visualisation of the deformed shapes of the axle and stabilizer bar. As illustrated in Figure 8, deformed configurations and contour plots of the deformation field can be displayed for selected instants of the response,

 doi:10.20944/preprints202512.0984.v1

providing an intuitive picture of the bending and twisting of the flexible components. Animations obtained from these simulations are supplied as supplementary video material, offering further insight into the dynamic behaviour of the test bench and the rear suspension assembly.

Finally, a dedicated force sensor located in the region of the right wheel spindle is used to record the reaction force transmitted by the test bench during the fatigue loading cycle. The resulting periodic signal exhibits a peak value of about 1 kN, which does not represent the maximum service load acting on the wheel, but the reaction corresponding to the prescribed displacement imposed by the bench, given the stiffness of the rear axle and suspension components. This peak value of the simulated reaction force is then adopted as an equivalent design load in the finite element analysis of the rear axle assembly, so that the boundary conditions in the structural model are fully consistent with the kinematic excitation and stiffness distribution represented in the multibody model.

The combination of multibody dynamics with flexible bodies therefore provides a comprehensive picture of the dynamic behaviour of the test bench. It allows the designer to verify that the mechanism operates without excessive kinematic amplification or undesired resonance, and at the same time supplies consistent internal force histories to be used as input for the subsequent explicit-dynamics finite element simulations of the rear axle housing and stabilizer bar.

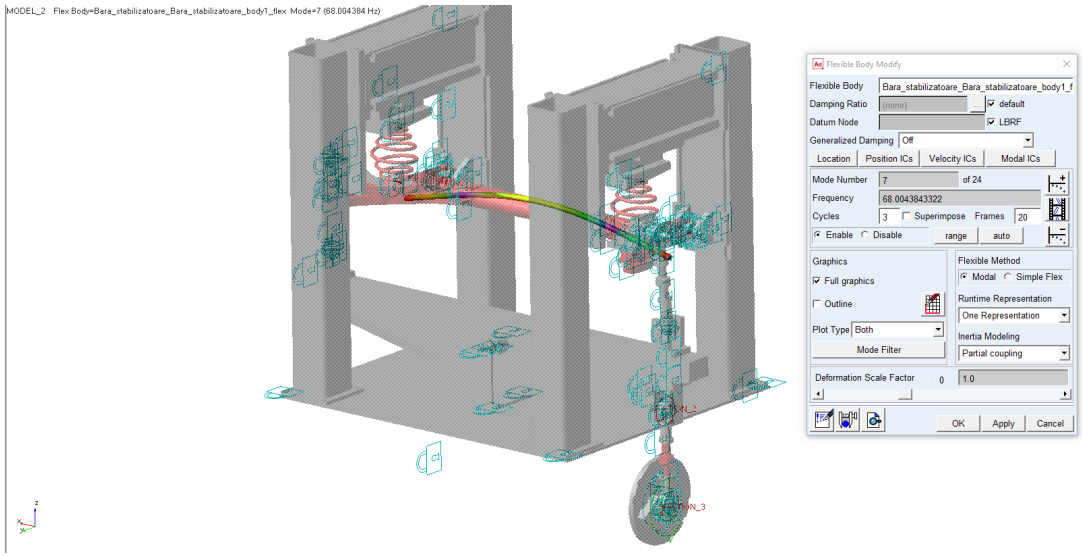

(**a**)

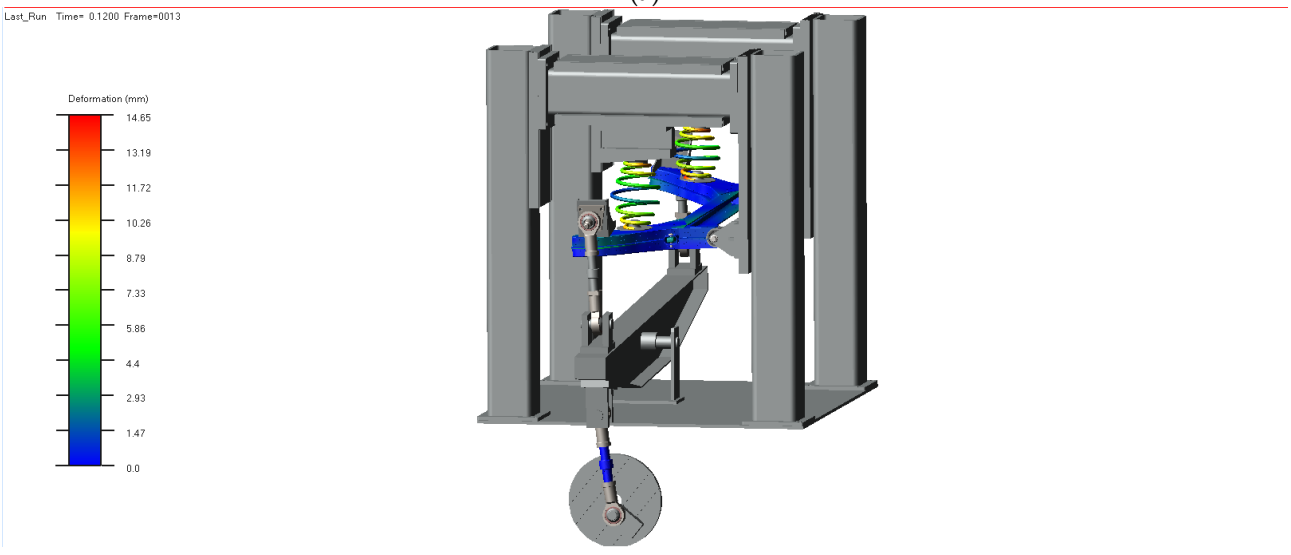

(**b**)

Figure 8. Visualisation of the flexible multibody model in MSC ADAMS: (a) definition and display of the deformed shape of the rear stabilizer bar as a flexible body; (b) contour plot of the deformation field of the rear axle–stabilizer assembly during dynamic excitation.

 doi:10.20944/preprints202512.0984.v1

4. Experimental Strain Analysis of the Rear Axle on the Test Bench

The numerical investigations presented in the previous sections were complemented by an experimental strain analysis carried out on the rear axle mounted on the durability test bench. The main objectives of this analysis were (i) to measure the strain and stress state in critical regions of the rear axle during the imposed fatigue loading cycle, and (ii) to provide reference data for the validation of the finite element model of the axle assembly.

4.1. Strain-Gauge Instrumentation and Measuring Points

The instrumentation layout on the rear axle is shown schematically in Figure 9. A total of nine measuring points were selected based on the fatigue-sensitive regions identified in previous studies and on the expected bending and torsion modes of the axle beam.

In the central portion of the axle beam, a strain-gauge rosette consisting of three grids was bonded on the tensile side of the beam (points 1, 2 and 3). The grids are oriented at different angles with respect to the longitudinal axis X of the beam so as to enable the reconstruction of the local principal strains and stresses under combined bending and torsion.

Additional single strain gauges were mounted in the following locations:

- Left beam head (points 4 and 5), in the vicinity of the left wheel-spindle region, to capture the local bending and torsional effects close to the left support;
- Right beam head (points 6 and 7), in a position geometrically symmetric to points 4 and 5 with respect to the mid-span of the axle beam, so that the stress state at both beam ends can be compared under the symmetric loading generated by the test bench;
- Left and right trailing arms (points 8 and 9), at the transitions between the bent sheet-metal arms and the axle beam, where geometric discontinuities may induce stress concentration even under globally symmetric excitation.

The X-axis of the local coordinate system is aligned with the longitudinal axis of the axle beam, while the Y-axis is oriented transversely, as indicated in Figure 9. This convention is consistent with the multibody and finite element models, which simplifies the comparison between measured and simulated stress components.

The layout of the nine strain-gauge measuring points on the rear axle and several details of the instrumentation are shown in Figure 9, a.

A photograph of the rear axle mounted on the test bench, with the strain-gauge positions indicated, is presented in Figure 9, d.

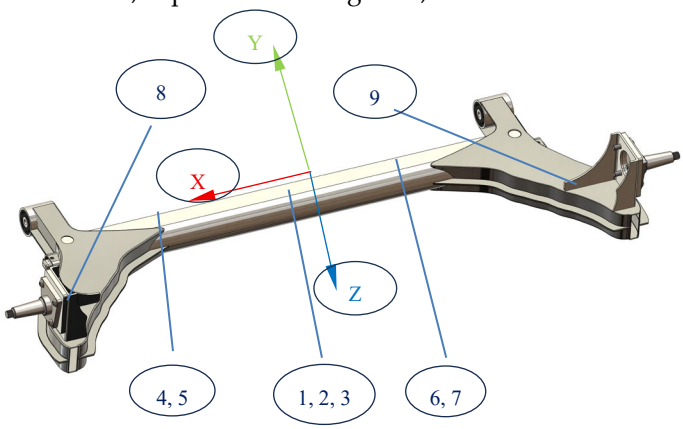

(**a**)

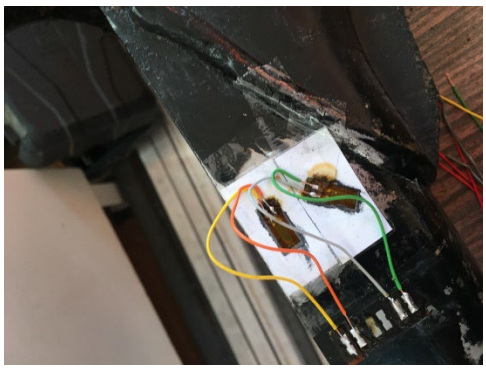

(**b**)

 doi:10.20944/preprints202512.0984.v1

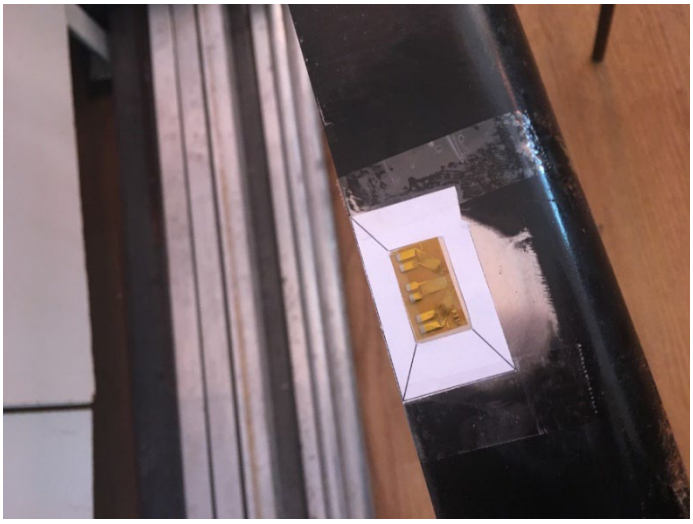

(**c**)

(**d**)

Figure 9. Experimental strain-gauge instrumentation of the rear axle: (**a**) CAD model of the axle with the global *X-Y-Z* axes and the locations of the nine measuring points (1–9); (**b**) single strain gauge mounted on the axle beam/head; (**c**) strain-gauge rosette bonded at mid-span of the axle beam; (**d**) rear axle installed on the test bench, with the instrumented regions and wiring visible.

A detailed view of the strain-gauge rosette bonded near the transition between the axle beam and the trailing arm is shown in Figure 9b. The three grids are oriented at different angles with respect to the beam axis and are protected with adhesive and epoxy coating, while the colour-coded lead wires are routed towards the data acquisition system.

4.2. Data Acquisition System and Measured Channels

The strain gauges were connected to an HBM MGCplus data acquisition system equipped with CANHEAD modules, providing stable bridge excitation, high-accuracy amplification and simultaneous multi-channel recording. The measurement set-up was configured to record both the input force in the driving mechanism and the mechanical stresses derived from the strain-gauge signals.

The experimental setup employed the following instrumentation:

- Force transducer S9M-50 kN (HBM, serial no. 31421930/2016), nominal force range ±50 kN, nominal sensitivity 2 mV/V, accuracy class 0.1, linearity ≤0.1 %. The sensor was conditioned by strain-gauge input modules SCM5B38-37 (Dataforth) with ±5 V output, nominal sensitivity 2 mV/V, 4 Hz bandwidth, linearity 0.01 % and continuous isolation of 240 Vrms.
- Reference force transducer U2B-50 kN (HBM, serial no. 168854/013481), nominal force range ±50 kN, nominal sensitivity 2 mV/V, accuracy class 0.5, coupled with an electronic indicator SCOUT55 (HBM, serial no. 827419902), used for calibration of the main force channel.
- Precision vernier caliper (MIB), measuring range 0–300 mm, resolution 0.01 mm (serial no. GX 140110211), used for checking geometric dimensions and sensor positioning.
- Portable data acquisition system SoftronicDataAcquisition, based on LAN-XI 3053B120 and LAN-XI 3160A042 modules, providing 16 analogue input channels, 2 analogue output channels (signal generator), one LAN port, one stabilised 5 V DC output and one stabilised 24 V DC output, with battery operation for up to 5 h with all acquisition systems active.

 doi:10.20944/preprints202512.0984.v1

- Strain gauges LY6-10/350 (HBM), resistance 350 Ω, gauge length 10 mm, gauge width 5 mm, polyamide backing, constantan grid, gauge factor k=2, used in quarter-bridge configurations.
- MGCplus data acquisition system (HBM), 15 measurement channels, maximum sampling frequency 19.2 kHz, accuracy 0.0025, used as the main multi-channel bridge amplifier.
- CANHEAD Data Acquisition System (HBM), strain-gauge measurement system in quarter-bridge configuration, 10 input channels, accuracy class 0.1, maximum sampling frequency 100 Hz.

Data acquisition and online signal processing were performed using Catman software (HBM), which provides real-time control, visualisation and multi-channel processing for MGCplus and CANHEAD systems.

The following quantities were recorded during the tests:

- Longitudinal force in the connecting link 2: F_link2 (N);
- Normal stress at mid-span of the axle beam, gauge oriented at−90◦ with respect to the OX axis: Sigma 1 (MPa);
- Normal stress at mid-span of the axle beam, gauge oriented at −135◦ with respect to the OX axis: Sigma 2 (MPa);
- Normal stress at mid-span of the axle beam, gauge oriented at −45◦ with respect to the OX axis: Sigma 3 (MPa);
- Normal stress at the left beam head, gauge oriented at 0◦ with respect to the OX axis: Sigma 4 (MPa);
- Normal stress at the left beam head, gauge oriented at −135◦ with respect to the OX axis: Sigma 5 (MPa);
- Normal stress at the right beam head, gauge oriented at 0◦ with respect to the OX axis: Sigma 6 (MPa);
- Normal stress at the right beam head, gauge oriented at −135◦ with respect to the OX axis: Sigma 7 (MPa);
- Normal stress in the left axle arm, gauge oriented at −45◦ with respect to the OX axis: Sigma 8 (MPa);
- Normal stress in the right axle arm, gauge oriented at −135◦ with respect to the OX axis: Sigma 9 (MPa).

The sampling frequency was chosen to ensure a sufficiently dense discretisation of the loading cycle, given the excitation frequency imposed in the ADAMS model and on the test bench (Section 3). All signals were recorded simultaneously during the start-up and steady-state operation of the bench.

The complete experimental setup, including the rear axle mounted on the test bench and the data-acquisition chain, is shown in Figure 10.

 doi:10.20944/preprints202512.0984.v1

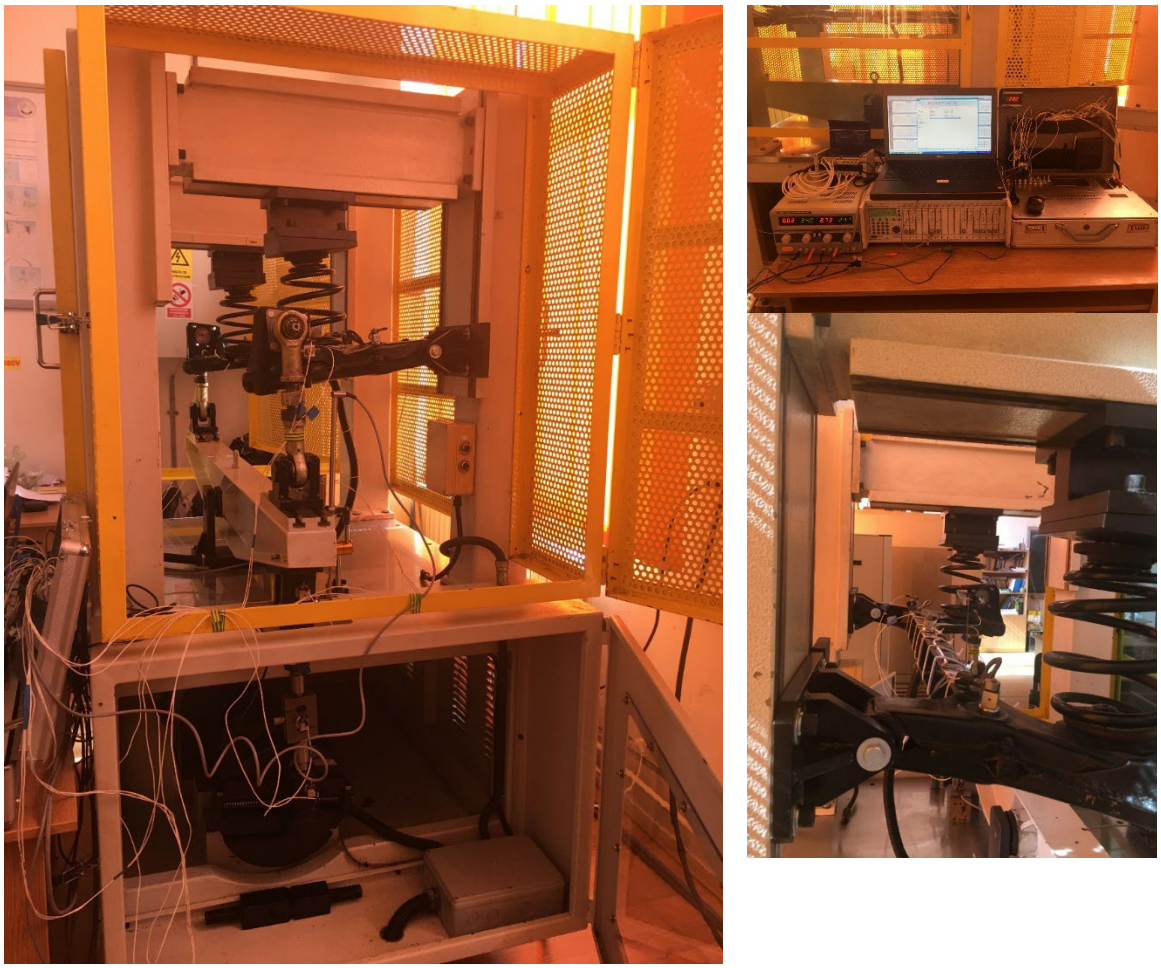

(**a**) (**b**)

Figure 10. Experimental setup for the strain measurements on the rear axle: (**a**) rear suspension durability test bench with the axle mounted and instrumented with strain gauges, inside the protective enclosure; (**b**) data acquisition and signal conditioning equipment together with a close-up view of the instrumented rear axle and coil springs inside the test bench.

4.3. Test Procedure and Data Processing

The experimental tests were carried out under the same operating conditions as those used in the multibody simulations, i.e., with the crank rotating at constant angular speed and the rocker beam imposing a periodic displacement on the right wheel-spindle region. After the stand was brought to operating speed, several consecutive cycles were recorded.

For the analysis, three load cycles (cycles 3, 4 and 5) were selected from the stabilised regime, after the decay of the initial transient. For each of these cycles and for each channel (F_Rod and Sigma 1–9), the following quantities were computed:

- mean value;
- root-mean-square (RMS) value;
- maximum value;
- minimum value.

The statistical processing was then extended across the three cycles:

- the average and standard deviation of the mean values and RMS values,
- the average and standard deviation of the maxima and minima,
- the peak-to-peak amplitude (difference between maximum and minimum) for each measured signal.

These results are summarised in Table 1, which reports the processed values for the connecting-rod force and for all nine stress channels. The relatively small standard deviations confirm the good

 doi:10.20944/preprints202512.0984.v1

repeatability of the measurements in the stabilised regime and indicate that the test bench operates under stable kinematic and loading conditions.

The strain-gauge bridges were configured and calibrated in Catman using the nominal resistance and gauge factor of the LY6-10/350 sensors (350 Ω, k=2) and the quarter-bridge wiring. The raw voltage signals were first converted into engineering strain $\varepsilon(t)$) for each channel. Assuming linear–elastic, isotropic behaviour of the axle material, the measured strains were then transformed into mechanical stresses by applying Hooke's law with a Young's modulus E=210 GPa (Poisson's ratio ν=0.3). For the single gauges, the stress in the gauge direction was obtained as $\sigma(t)=E\,\varepsilon(t)$, so that each channel Sigma 1–9 directly represents the normal stress in MPa along the orientation of the corresponding strain gauge. In the case of the strain-gauge rosette mounted at mid-span of the beam, the three measured strains were combined to reconstruct the in-plane strain components and the associated normal stresses in the chosen directions, which are likewise reported as Sigma 1–3.

Figure 11 shows the strain histories recorded by the three grids of the rosette mounted at mid-span of the axle beam. After an initial idle phase, the stand is brought to operating speed at about t≈9 s, where the signals quickly reach a steady-state, nearly sinusoidal regime that is maintained up to approximately t≈38 s. The subsequent increase and decay of the amplitudes correspond to the controlled run-down of the stand at the end of the test. It can be observed that channel 1 exhibits only small strain amplitudes, whereas channels 2 and 3 reach significantly higher values, indicating that the dominant bending and torsional stresses in the mid-span region are aligned closer to the−135◦ and −45◦ directions with respect to the beam axis. The stabilised part of these records (cycles 3–5 in the steady-state window) was used for the statistical processing summarised in Table 1.

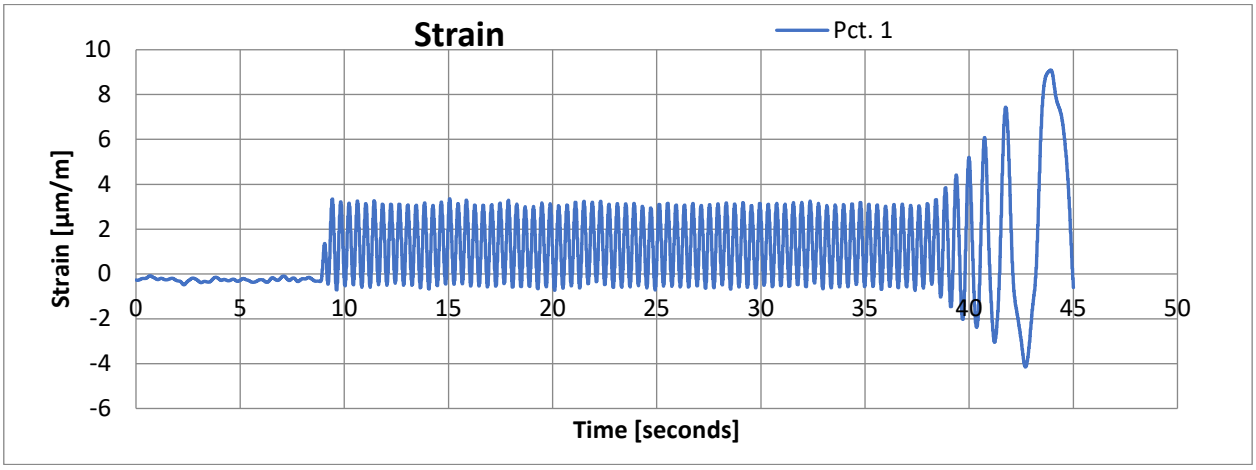

(**a**)

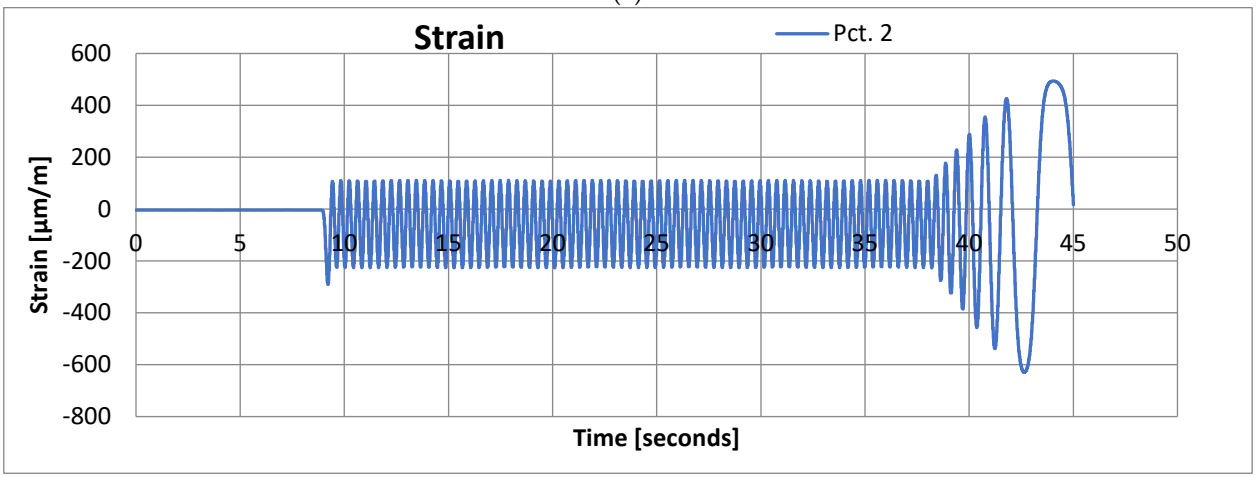

(**b**)

 doi:10.20944/preprints202512.0984.v1

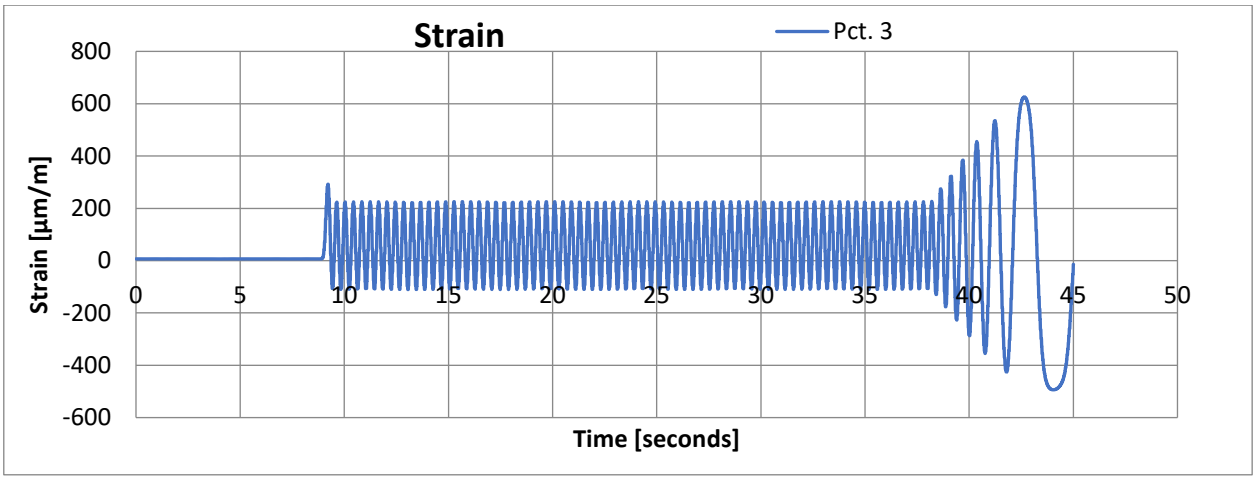

(**c**)

Figure 11. Time histories of the measured strains at mid-span of the axle beam (strain-gauge rosette): (a) point 1, gauge oriented at −90◦ to the OX axis; (b) point 2, gauge oriented at −135◦; (c) point 3, gauge oriented at −45◦.

To check the repeatability and stationarity of the loading cycle, the full time histories of the connecting-link force and of the nine stress channels were inspected in TestPoint. Figure 12 presents representative time windows taken from the beginning, from the middle and from the end of the measurement. In all three cases, the force and stress signals exhibit the same waveform, frequency and amplitude within the steady-state portion of the test, confirming that the stand reproduces an identical motion and load cycle throughout the entire recording and that no significant drift or degradation of the excitation occurs.

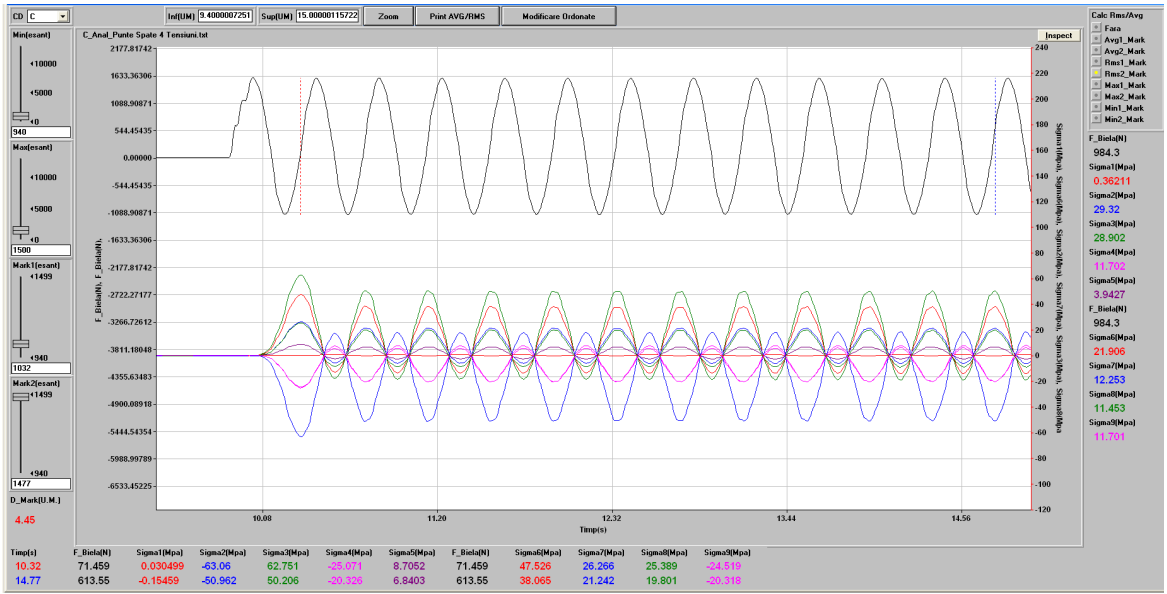

(**a**)

 doi:10.20944/preprints202512.0984.v1

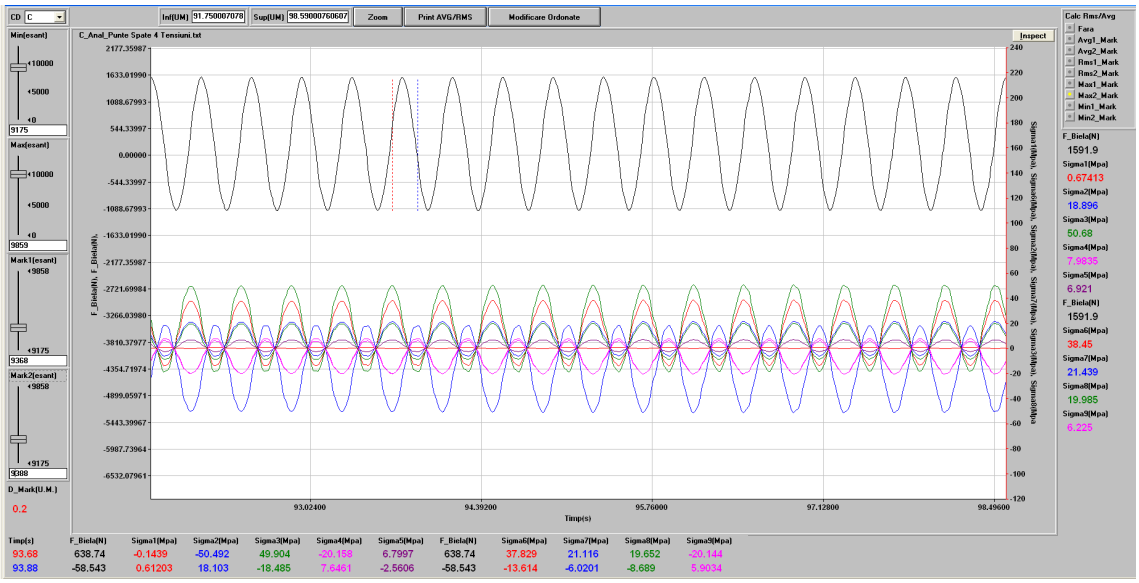

(**b**)

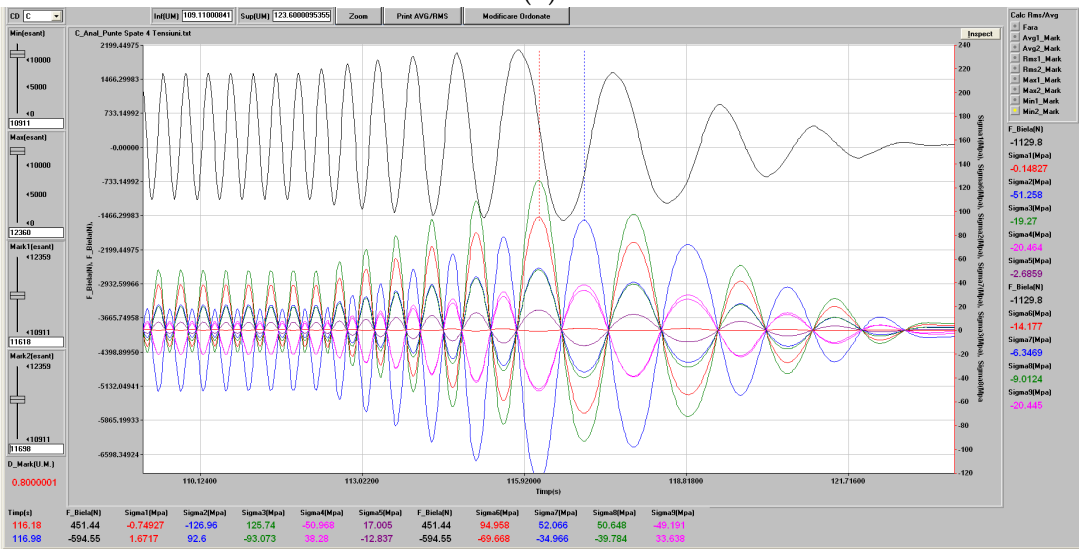

(**c**)

Figure 12. Multi-channel recordings from TestPoint for the rear axle fatigue test: (a) time window at the beginning of the stabilised regime; (b) time window in the middle of the recording; (c) time window at the end of the recording, including the stand run-down. The upper trace shows the connecting-link force, while the coloured curves represent the nine stress channels Sigma 1–9.

Table 1. Processed experimental results for the connecting-link force and the measured stresses at the nine strain-gauge locations on the rear axle (averages and peak-to-peak values over cycles 3–5).

	F_Rod	Sigma-1	Sigma-2	Sigma-3	Sigma-4	Sigma-5	Sigma-6	Sigma-7	Sigma-8	Sigma-9
	(N)	(MPa)	(MPa)	(MPa)	(MPa)	(MPa)	(MPa)	(MPa)	(MPa)	(MPa)
Medium value										
Cycle 3	230.66	0.25	-16.21	15.70	-6.24	2.11	12.11	7.53	5.48	-7.12
Cycle 4	232.41	0.25	-16.24	15.74	-6.25	2.12	12.14	7.54	5.49	-7.14
Cycle 5	230.65	0.25	-16.01	15.68	-6.21	2.11	12.10	7.52	5.48	-7.09
Average	231.24	0.25	-16.15	15.71	-6.24	2.11	12.12	7.53	5.48	-7.12
St.Dev	0.83	0.00	0.10	0.02	0.02	0.00	0.02	0.01	0.01	0.02
Value (RMS efficacy)										
Cycle 3	976.07	0.37	29.26	28.92	11.69	3.94	21.92	12.24	11.46	11.67
Cycle 4	976.54	0.37	29.28	28.94	11.69	3.94	21.93	12.25	11.47	11.68

 doi:10.20944/preprints202512.0984.v1

	F_Rod	Sigma-1	Sigma-2	Sigma-3	Sigma-4	Sigma-5	Sigma-6	Sigma-7	Sigma-8	Sigma-9
	(N)	(MPa)	(MPa)	(MPa)	(MPa)	(MPa)	(MPa)	(MPa)	(MPa)	(MPa)
Cycle 5	974.90	0.37	29.12	28.88	11.66	3.94	21.89	12.22	11.45	11.65
Average	975.84	0.37	29.22	28.91	11.68	3.94	21.91	12.24	11.46	11.67
St.Dev	0.69	0.00	0.07	0.03	0.02	0.00	0.02	0.01	0.01	0.01
					Maximum value					
Cycle 3	1591.95	0.67	18.94	50.74	8.01	6.92	38.45	21.46	20.00	6.23
Cycle 4	1591.72	0.67	18.93	50.74	8.01	6.92	38.44	21.46	20.00	6.22
Cycle 5	1591.07	0.68	19.13	50.65	8.03	6.93	38.41	21.43	20.01	6.26
Average	1591.58	0.68	19.00	50.71	8.02	6.93	38.43	21.45	20.00	6.24
St.Dev	0.37	0.01	0.09	0.04	0.01	0.00	0.02	0.02	0.00	0.02
					Minimum value					
Cycle 3	-1131.29	-0.18	-51.44	-19.32	-20.56	-2.74	-14.25	-6.39	-9.10	-20.50
Cycle 4	-1131.29	-0.18	-51.40	-19.31	-20.55	-2.71	-14.23	-6.39	-9.07	-20.48
Cycle 5	-1131.59	-0.17	-51.15	-19.33	-20.46	-2.72	-14.25	-6.42	-9.06	-20.43
Average	-1131.39	-0.18	-51.33	-19.32	-20.52	-2.72	-14.25	-6.40	-9.08	-20.47
St.Dev	0.14	0.01	0.13	0.01	0.04	0.01	0.01	0.01	0.02	0.03
					Amplitude					
	2722.97	0.86	70.33	70.03	28.54	9.65	52.68	27.85	29.08	26.71

4.4. Measured Stress Levels and Identification of Critical Regions

Inspection of the recorded time histories shows that all stress channels exhibit a periodic variation consistent with the imposed cyclic loading. A typical example is provided in Figure 12, b, which illustrates the rod force and selected stress components over a representative cycle in the steady-state regime.

From Table 1, it can be observed that:

- the maximum recorded stresses in the mid-span region (Sigma 3 channel) reach values of approximately 50–51 MPa in the most heavily loaded parts of the cycle;
- stresses at the beam heads and arms are somewhat lower in magnitude, with typical maxima in the range of 20–40 MPa, depending on the location and orientation of the gauge;
- the peak-to-peak amplitudes of the stress signals (last line of Table 1) provide a direct indication of the cyclic stress range experienced at each measuring point, which is particularly relevant for fatigue assessment.

Although only nine points on the axle were instrumented, the measured stress distribution already suggests that the most critical regions under the considered loading cycle are located in the central portion of the beam and in the vicinity of the right beam head, where the excitation is applied on the test bench. This observation is consistent with previous numerical studies and will be further quantified by the finite element analysis presented in the next section.

It should be emphasised that in the experimental campaign the stress field is sampled only at discrete locations, limited by the number of strain gauges that can reasonably be installed on the axle. By contrast, finite element analysis provides full-field maps of stresses and strains over the entire structure. The comparison between the measured stresses at the instrumented points and the corresponding values predicted by the FE model therefore constitutes a crucial step in the validation of the numerical model and in the subsequent identification of stress concentration zones and potential fatigue-critical details.

 doi:10.20944/preprints202512.0984.v1

5. Finite Element Analysis of the Rear Axle Assembly

5.1. Geometry Preparation and FE Model

The finite element analysis was carried out in ANSYS Workbench, using the CAD assembly of the rear axle previously created in SolidWorks. The geometry was first imported into DesignModeler, where a series of clean-up operations were performed to ensure a robust mesh and physically meaningful connections between parts. In particular, small fillets and chamfers not affecting the global stiffness were removed, artificial overlaps were corrected and several adjacent sheet-metal components (U-shaped cross member, bent side arms and end brackets) were merged by Boolean operations into a single solid representing the rear axle beam.

The final model of the rear axle assembly contains the main torsion beam, the trailing arms, the wheel-spindle regions and the brackets for the springs and stabilizer bar. The components that are welded in the real structure are represented as a single continuous body, whereas components connected by bushings in the real suspension (e.g., body mounts) are modelled by appropriate boundary conditions. The mesh consists of 3D solid elements with local refinement in the vicinity of geometric discontinuities, such as the junction between the bent side plate and the bent arm, and around the locations of the strain gauges (points 1–9), in order to capture accurately the stress gradients in these critical regions.

The axle material is assumed to be structural steel with linear elastic behaviour, characterised by a Young's modulus E=210 GPa and Poisson's ratio ν=0.3. The rubber bushings that connect the axle to the vehicle body in service and to the stand in the laboratory are represented by equivalent linear springs and dashpots with stiffness and damping values consistent with the experimental stand. The Explicit Dynamics module of ANSYS Workbench was used in order to handle the contact conditions and the nonlinear stiffness of the bushings in a numerically stable way.

5.2. Boundary Conditions and Loading

The CAD geometry of the rear axle was imported into ANSYS DesignModeler as an assembly of solid bodies (torsion beam, side arms and spindle brackets). The parts that are welded in the real component were merged into a single continuous body, whereas those connected through bushings or supports were kept as separate entities to allow the definition of realistic boundary conditions. After this preprocessing step, the assembly was discretised with 3D solid elements, with mesh refinement in the vicinity of geometric discontinuities and in the wheel-spindle region (Figure 12b). The supports corresponding to the axle bushings and spring seats were constrained to reproduce the mounting conditions on the test bench, and a vertical force was applied at the wheel spindle (Figure 12a), consistent with the equivalent reaction obtained from the multibody simulation.

 doi:10.20944/preprints202512.0984.v1

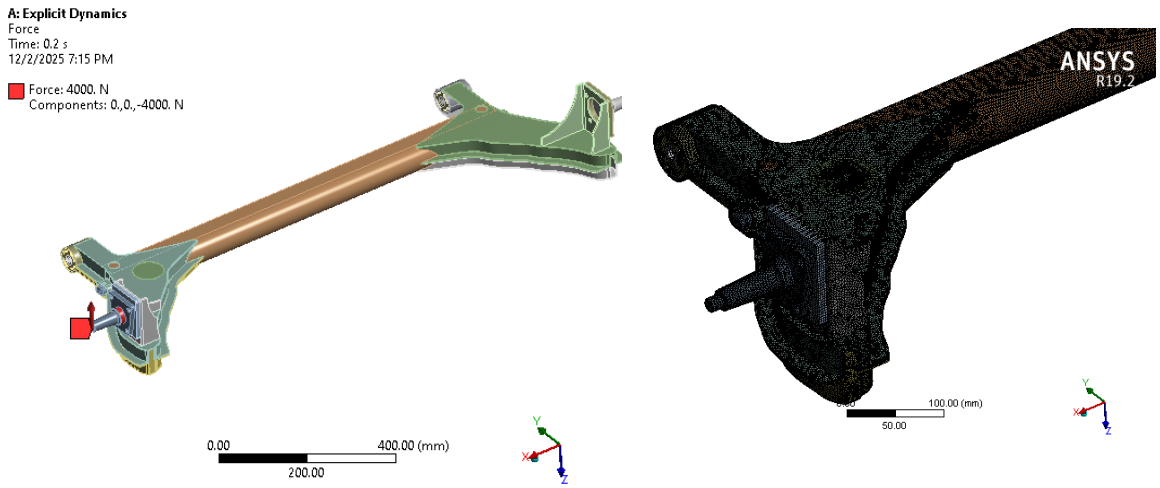

(**a**) (**b**)

Figure 13. Finite element model of the rear axle assembly in ANSYS Explicit Dynamics: (a) geometry of the axle and wheel-spindle region imported in DesignModeler, with the vertical force applied at the spindle; (b) detail of the solid finite element mesh in the right-hand arm and spindle area.

The explicit dynamic analysis was run over one complete loading cycle, with a time step automatically controlled by the stability criterion of the solver. The resulting time histories of displacements, strains and stresses were post-processed at the nodes corresponding to the experimental measuring points, as well as over the entire axle surface to obtain full-field stress maps.

5.3. Stress Distribution and Critical Regions

The von Mises equivalent stress distribution at the instant of maximum load reveals that the most highly stressed region is the corner area where the bent side plate joins the bent side arm, on the side of the axle where the excitation is applied. In this region, the equivalent stress reaches a maximum of approximately 104 MPa, as illustrated in the contour plots of the FE results. This corner therefore represents a potential fatigue-critical detail and a prime candidate for design optimisation (e.g., by introducing larger radii or local stiffening).

In the central portion of the axle beam, the equivalent stresses are significantly lower but still non-negligible. The FE model predicts a maximum equivalent stress of about 54.6 MPa at the mid-span of the U-shaped cross member, decreasing to approximately 41 MPa in the adjacent areas. These values are consistent with the expectation that the central region is mainly subjected to global bending and torsion rather than to strong local stress concentrations.

The stress levels in the regions corresponding to the strain gauges at the beam heads (points 4–7) and in the trailing arms (points 8–9) are lower than in the aforementioned hot spots but still relevant to fatigue. In particular, the FE analysis yields equivalent stresses of about 27 MPa in the vicinity of points 4–5 and about 41 MPa near points 6–7. Although these locations are geometrically symmetric with respect to the beam mid-span, the local stress values differ because of the complex geometry of the brackets and the presence of additional stiffening features, which slightly modify the local stiffness and stress flow. The stresses in the trailing arms (points 8–9) are smaller, in line with the more compliant geometry and with the larger distance from the main load path.

Overall, all predicted stresses remain well below the yield strength of the axle material for the considered equivalent design load, indicating a comfortable static safety margin. However, the local maxima and the stress gradients identified by the FE analysis are highly relevant for assessing fatigue strength and for guiding possible design improvements.

 doi:10.20944/preprints202512.0984.v1

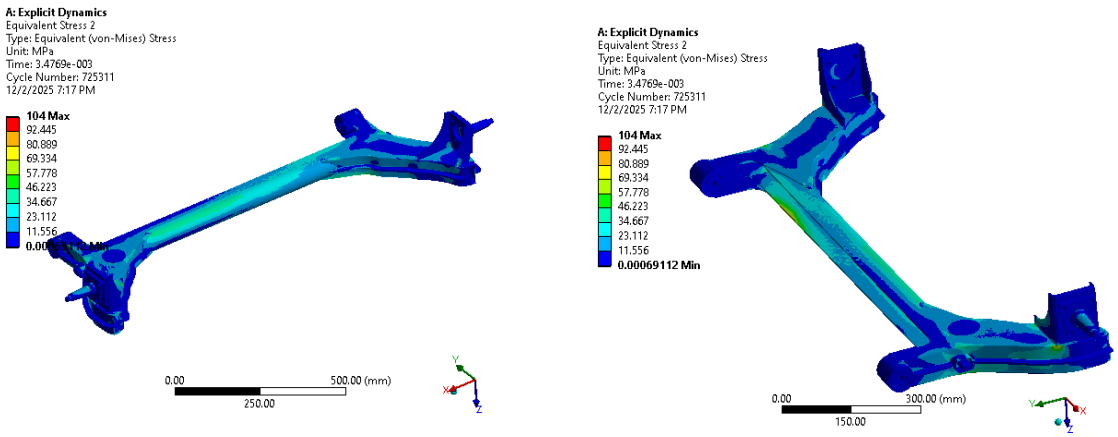

(**a**) (**b**)

Figure 14. Equivalent (von Mises) stress in the rear axle at the instant of maximum applied load from the explicit dynamic analysis: (a) overall view of the axle; (b) enlarged view of the right-hand arm and spindle region, highlighting the local stress concentration.

The von Mises stress field at the instant of maximum applied load is shown in Figure 14. The overall view in Figure 14a indicates that the stress distribution is far from uniform: most of the axle beam is subjected to moderate equivalent stresses below about 60–70 MPa, while significantly higher values appear in the transition regions between the main beam and the side arms. The detailed view in Figure 14b reveals a pronounced local maximum in the corner where the right-hand arm joins the beam and spindle bracket, with a peak equivalent stress of approximately 104 MPa. This confirms that the welded junction between the bent side plate and the arm is the most critical area of the axle for the considered loading case and should be regarded as a potential fatigue hot spot in any subsequent design optimisation.

5.4. Correlation with Experimental Strain Measurements

To validate the finite element model, the stress results at the nodes corresponding to the strain-gauge locations were compared with the experimental values derived from the strain measurements presented in Section 4. For the central portion of the beam, the stresses obtained from the rosette gauges (channels Sigma 1–3) reach peak values of approximately 50.7 MPa during the stabilised cycles. This is in very good agreement with the FE prediction of about 54.6 MPa at the same location, the difference being within roughly 10%.

At the beam heads, the experimentally derived stresses in points 4–7 are also of the same order of magnitude as those predicted numerically. The FE model tends to slightly overestimate the stresses on the side where stronger geometric discontinuities are present, which is expected for a model that neglects certain local compliance effects (e.g., small gaps, weld toe geometry). In the trailing arms (points 8–9), both experiment and simulation confirm relatively low stress levels, confirming that these regions are not critical for the current loading case.

The overall comparison shows that the finite element model reproduces well both the absolute levels and the relative distribution of stresses along the axle. The FE analysis correctly identifies the same critical regions suggested by the strain-gauge measurements, while providing a full-field view of the stress and strain state that cannot be obtained experimentally. This agreement gives confidence that the combined multibody–FE approach can be used as a reliable tool for evaluating alternative axle designs and for optimising the geometry with respect to fatigue strength.

We perform the FE analysis in order to extend the information obtained from the discrete strain-gauge measurements to the entire axle, identifying stress concentrations and critical regions that cannot be accessed experimentally and providing a reliable basis for fatigue assessment and design optimisation.

 doi:10.20944/preprints202512.0984.v1

The comparison between measured and simulated stresses shows a very good agreement, with differences of about 10% at the beam mid-span and the same order of magnitude at all other instrumented points, confirming that the FE model faithfully reproduces both the absolute stress levels and their distribution along the axle.

6. Design Optimisation of the Rear Axle Wheel Spindle

The results presented in the previous sections show that, for the considered loading case, the highest equivalent stresses are concentrated in the junction regions between the beam, side arms and spindle brackets. Among all components of the rear axle, the wheel spindle, which supports the hub and wheel bearings, is the most safety-critical part: a fracture of the spindle would lead to the loss of the wheel and therefore to a potentially catastrophic failure of the vehicle. For this reason, the spindle is selected as the primary target for design optimisation.

The purpose of this section is to use the validated finite element model as a basis for refining the geometry of the spindle region, with the dual objective of:

- reducing the maximum local stresses and stress gradients in the spindle and its immediate vicinity, thus increasing the fatigue strength and safety margin, and
- preserving the global stiffness and mass characteristics of the axle assembly, so that the overall kinematic and dynamic behaviour of the suspension is not adversely affected.

To this end, the FE model is restricted to the substructure containing the spindle, the adjacent portion of the arm and the beam–arm junction, while the boundary conditions are inherited from the full-axle model (displacements and reaction forces applied on the cut boundaries). The optimisation problem is formulated in terms of a small number of geometric design variables (for example, fillet radii, local thicknesses and transition angles around the spindle base), with the objective of minimising the peak von Mises stress in the spindle region, subject to constraints on mass, stiffness and manufacturability.

In the following subsections, the design variables, objective function and constraints are specified, and the numerical procedure adopted for the iterative FE-based optimisation of the spindle is described.

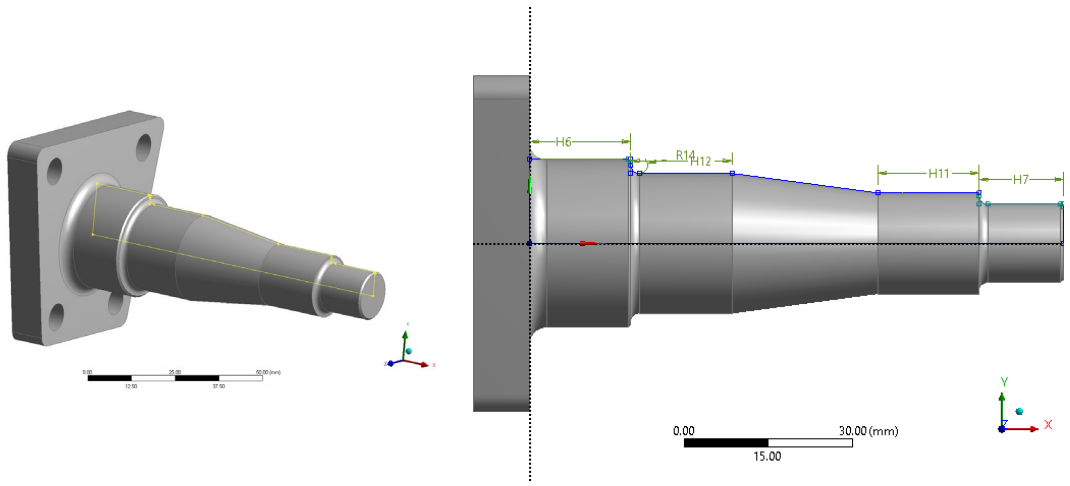

(**a**) (**b**)

 doi:10.20944/preprints202512.0984.v1

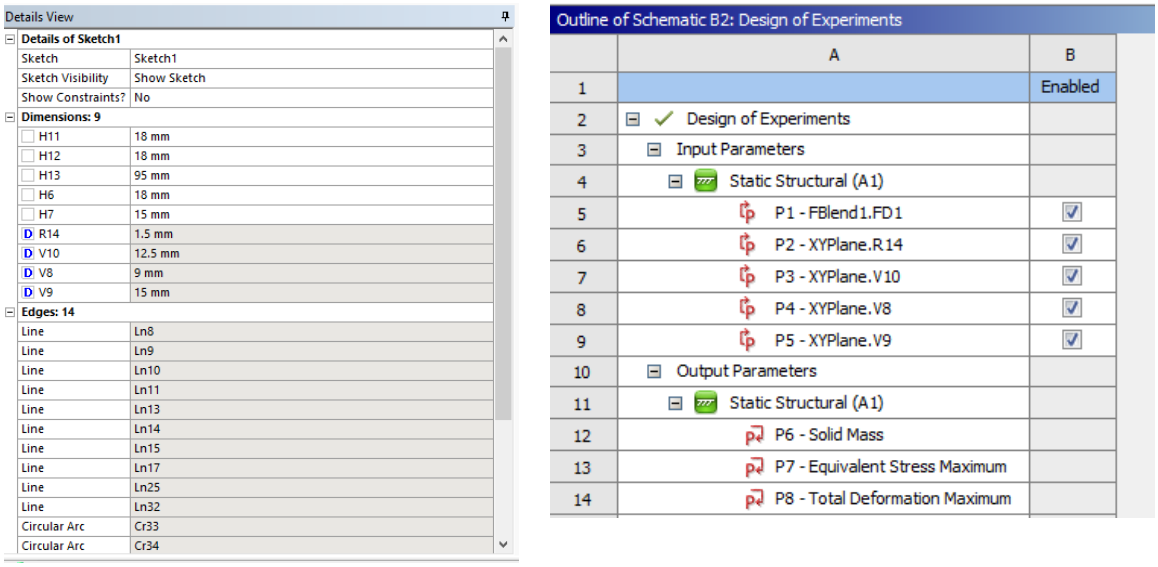

Details View

Details of Sketch1	
Sketch	Sketch1
Sketch Visibility	Show Sketch
Show Constraints?	No
Dimensions: 9	
H11	18 mm
H12	18 mm
H13	95 mm
H6	18 mm
H7	15 mm
R14	1.5 mm
V10	12.5 mm
V8	9 mm
V9	15 mm
Edges: 14	
Line	Ln8
Line	Ln9
Line	Ln10
Line	Ln11
Line	Ln13
Line	Ln14
Line	Ln15
Line	Ln17
Line	Ln25
Line	Ln32
Circular Arc	Cr33
Circular Arc	Cr34

(c)

Outline of Schematic B2: Design of Experiments

	A	B
1		Enabled
2	Design of Experiments	
3	Input Parameters	
4	Static Structural (A1)	
5	P1 - FBlend1.FD1	☑
6	P2 - XYPlane.R14	☑
7	P3 - XYPlane.V10	☑
8	P4 - XYPlane.V8	☑
9	P5 - XYPlane.V9	☑
10	Output Parameters	
11	Static Structural (A1)	
12	P6 - Solid Mass	
13	P7 - Equivalent Stress Maximum	
14	P8 - Total Deformation Maximum	

(d)

Figure 15. Parametric setup of the wheel spindle in ANSYS Workbench: (a) 3D CAD model of the spindle with the bearing seats and mounting flange; (b) 2D profile sketch with the main dimensional constraints; (c) list of geometric parameters defined in Details of Sketch (diameters, fillet radius and axial lengths); (d) Design of Experiments table linking the input parameters (P1–P5) to the output responses (solid mass, maximum equivalent von Mises stress and maximum total deformation).

The optimisation is focused on the geometry of the wheel spindle, which was modelled as a separate, fully parametric component in ANSYS DesignModeler (Figure 15). The sketch defining the spindle profile includes a set of key dimensions – axial lengths $H11$–$H13$, diameters $V8$–$V10$ and fillet radius $R14$ – that control the bearing seats, the transition between different sections and the connection to the mounting flange. These dimensions were exposed as design parameters in Workbench and subsequently used as design variables in the response-surface-based optimisation procedure.

The optimisation of the wheel spindle was performed in ANSYS Workbench using the parametric workflow illustrated in Figure 16. First, a Static Structural system (A) was set up, in which the spindle geometry, material data, boundary conditions and loads were defined as in the validated FE model, and a set of key geometric dimensions of the spindle region were promoted as design parameters. These parameters were collected in the Parameter Set and linked to a Response Surface system (B). A Design of Experiments (DoE) was then generated to sample the design space; for each design point, the static analysis was solved and the resulting maximum von Mises stress in the spindle and the corresponding mass were stored as responses.

Based on these results, ANSYS built a response surface metamodel, which was subsequently used in the Response Surface Optimization system (C) to search for the best combination of design parameters. The optimisation objective was to minimise the peak von Mises stress in the spindle region, while imposing constraints on the component mass and on selected stiffness-related quantities, so that the global behaviour of the rear axle remains compatible with the original design.

 doi:10.20944/preprints202512.0984.v1

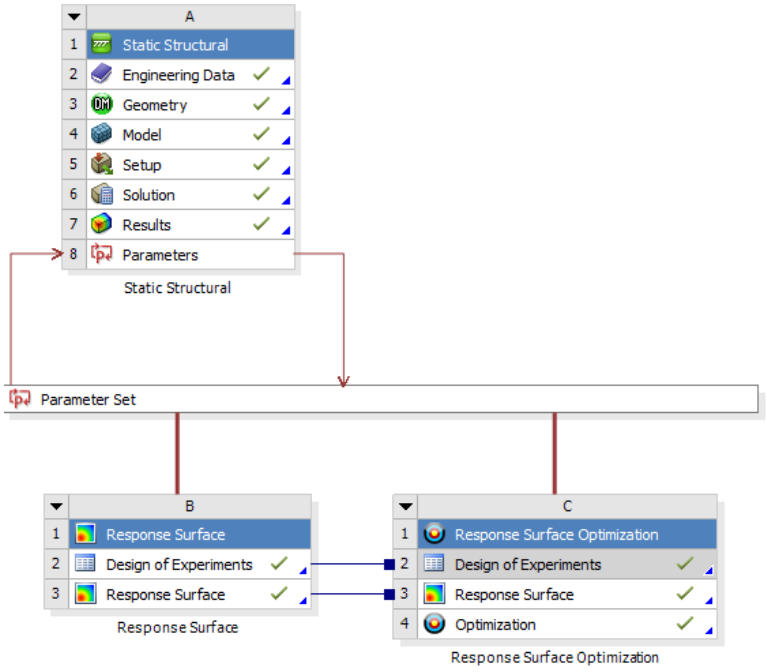

(**a**)

Figure 16. ANSYS Workbench workflow used for the wheel spindle optimisation: parametric Static Structural analysis (A), construction of the response surface based on a design of experiments (B) and response-surface-based optimisation (C).

In the Design of Experiments module, five input parameters were defined, corresponding to the most influential geometric dimensions of the spindle (Figure 15d). Parameter P1 controls the axial blend length at the transition between the flange and the first bearing seat (Blend1.FD1). Parameters P2 and P3 correspond to the fillet radius $R14$ and to the diameter $V10$ of the central section of the spindle, respectively, while parameters P4 and P5 define the diameters $V8$ and $V9$ of the adjacent sections. These parameters were varied within practical bounds dictated by bearing dimensions, assembly requirements and manufacturability.

For each design point in the DoE, the static analysis was solved and three output responses were recorded: P6 – the solid mass of the spindle, P7 – the maximum equivalent von Mises stress in the spindle region, and P8 – the maximum total deformation at the critical nodes. In the subsequent response-surface optimisation, P7 was taken as the objective function to be minimised, while P6 and P8 were used as constraints to ensure that the optimised design does not lead to an unacceptable increase in mass or a reduction in stiffness with respect to the baseline spindle.

The design space explored in the optimisation is defined by the five geometric parameters listed in Table 2. Parameter $P1$ controls the axial length of the blend between the flange and the first bearing seat, while $P2$ specifies the fillet radius at the same junction. Parameters $P3$, $P4$ and $P5$ correspond to the diameters of the central, intermediate and outer spindle sections, respectively, and therefore govern both the local stiffness and the mass of the component. The minimum and maximum levels were selected around the nominal (central) values so as to respect bearing and seal fit requirements, available packaging space and manufacturing constraints, while still allowing sufficient variation to reveal the sensitivity of stress, deformation and mass to each parameter.

Table 2. Design-of-experiments (DoE) input parameters used for the wheel spindle optimisation.

Parameter	ANSYS label	Central value	Minimum level	Maximum level	Unit	Description
P1	Blend1.FD1	3.0	2.7	3.3	mm	Axial blend length at transition

 doi:10.20944/preprints202512.0984.v1

						between flange and first bearing seat
P2	R14	1.5	1.35	1.65	mm	Fillet radius at junction between flange and spindle
P3	V10	12.5	12.146	12.854	mm	Diameter of the central spindle section
P4	V8	9.0	8.745	9.255	mm	Diameter of the section adjacent to the flange
P5	V9	15.0	13.5	16.5	mm	Diameter of the outer spindle section (near the wheel bearings)

The response surfaces in Figure 17 show how the maximum total deformation of the spindle varies with the selected geometric parameters. In Figure 17a, a shallow minimum of *P*8 is observed close to the central values of the blend length *P*1 and fillet radius *P*2; moving towards the lower or upper bounds of these parameters leads to a slight increase in deformation, indicating that excessively small or large transition lengths and fillet radii reduce the local stiffness of the spindle. Figure 16b highlights a stronger influence of the central diameter *P*3: decreasing *P*3 and *P*1 simultaneously produces the largest deformations, whereas combinations with larger diameters and longer blends yield a stiffer spindle. Overall, the surfaces confirm that the candidate design space contains a region where the deformation remains close to the baseline value, which is used as a constraint in the optimisation to avoid an undesirable loss of stiffness.

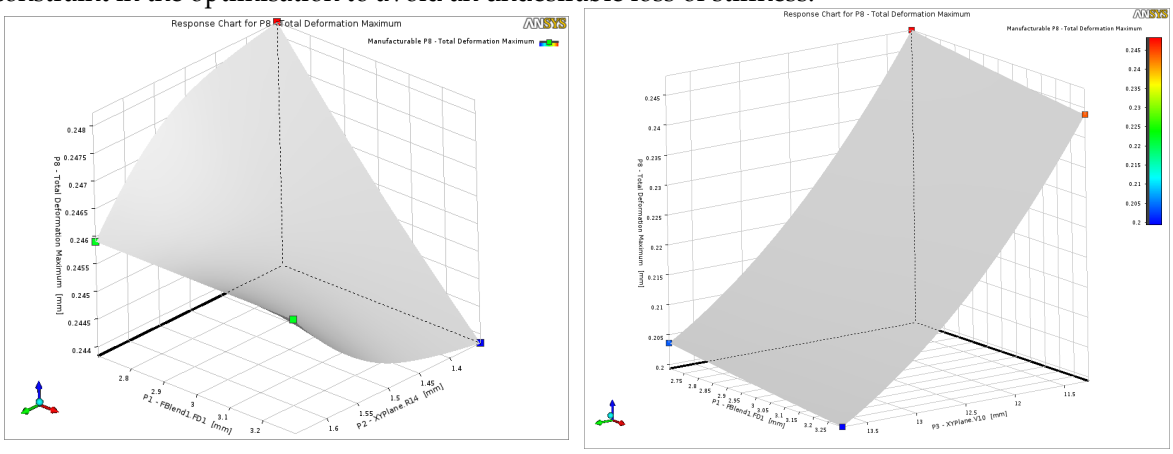

(**a**) (**b**)

Figure 17. Response surfaces for the maximum total deformation *P*8 of the wheel spindle obtained from the DoE: (a) effect of the axial blend length *P*1 (Blend1.FD1) and fillet radius *P*2 (R14); (b) effect of the axial blend length *P*1 and the central diameter *P*3 (V10).

The influence of the geometric parameters on the maximum equivalent von Mises stress is illustrated by the response surfaces in Figure 18. In Figure 18a, the stress level decreases when both the blend length *P*1 and the fillet radius *P*2 are increased, indicating that smoother and more gradual transitions between the flange and the spindle significantly reduce the local stress concentration. The lowest stresses are obtained near the upper bounds of *P*1 and *P*2, whereas the most compact geometry (short blend and small radius) leads to the highest stresses.

Figure 18b shows a pronounced dependence on the central diameter *P*3: increasing *P*3 results in a marked reduction of the maximum stress, while smaller diameters yield higher stress levels even if *P*1 is increased. This confirms that both the cross-sectional area and the transition geometry play an

 doi:10.20944/preprints202512.0984.v1

important role in controlling the peak stresses in the spindle region. Consequently, the optimisation process favours combinations with slightly larger diameters and generous transition blends, within the constraints imposed by bearing fit and overall packaging.

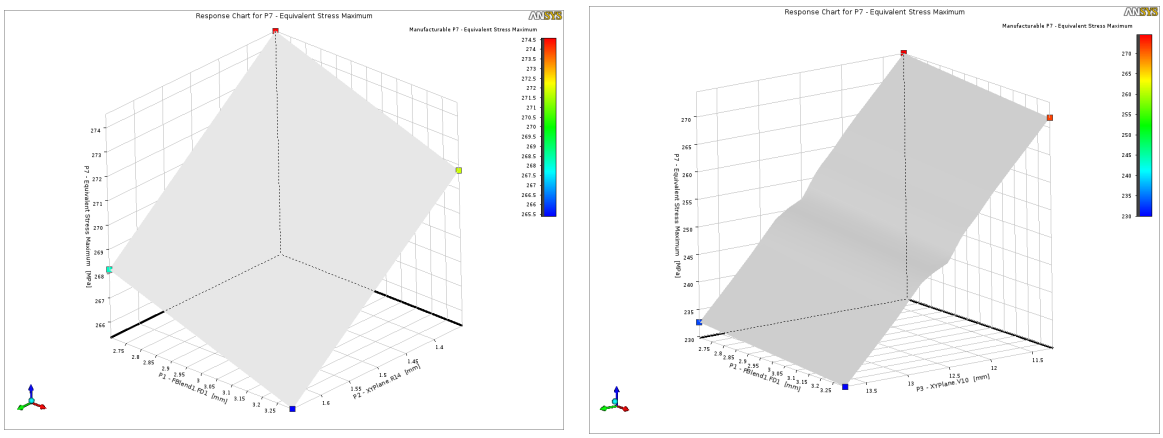

(**a**) (**b**)

Figure 18. Response surfaces for the maximum equivalent von Mises stress *P*7 in the wheel spindle: (**a**) combined effect of axial blend length *P*1 (Blend1.FD1) and fillet radius *P*2 (R14); (**b**) combined effect of axial blend length *P*1 and central diameter *P*3 (V10).

The influence of the design variables on the spindle mass is shown in Figure 19. In Figure 19a, the response surface exhibits a shallow bowl-shaped profile, indicating that variations of the blend length *P*1 and fillet radius *P*2 within the selected bounds have only a modest effect on the solid mass *P*6. Increasing *P*1 and *P*2 simultaneously leads to a slight mass increase, whereas the smallest values yield the lightest but also the most highly stressed designs. Figure 19b reveals that the mass is much more sensitive to the central diameter *P*3: reductions of *P*3 produce a noticeable mass saving, while larger diameters increase *P*6 almost linearly. These trends confirm that the optimisation must balance the beneficial effect of larger diameters and generous blends on stress reduction against the associated penalty in mass, which is enforced in the optimisation as an upper bound on *P*6.

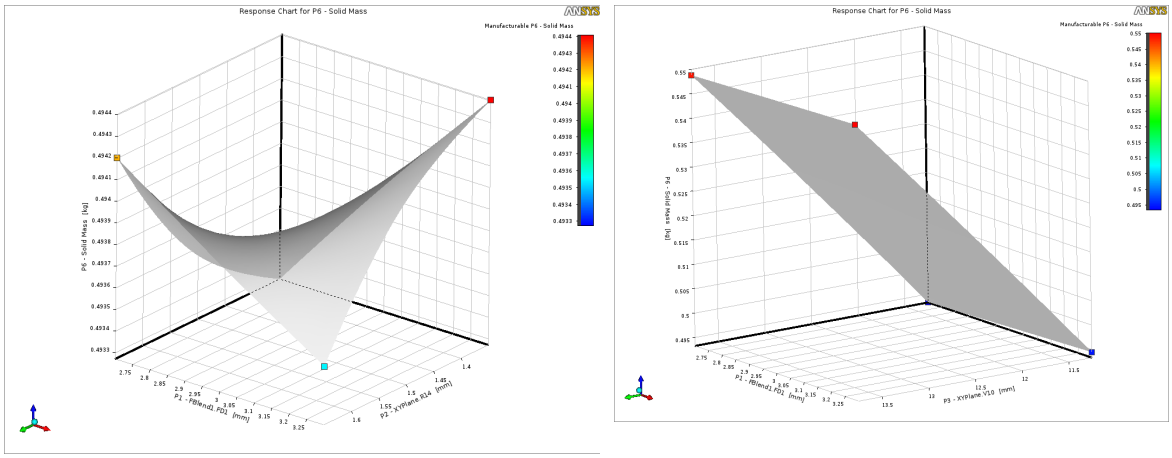

(**a**) (**b**)

Figure 19. Response surfaces for the spindle solid mass *P*6: (**a**) combined effect of axial blend length *P*1 (Blend1.FD1) and fillet radius *P*2 (R14); (**b**) combined effect of axial blend length *P*1 and central diameter *P*3 (V10).

The analysis of the response surfaces confirms that the geometric parameters selected for the spindle have a clear and physically meaningful influence on all three output quantities. Larger blend length *P*1 and fillet radius *P*2 systematically reduce the maximum equivalent stress, with only a

 doi:10.20944/preprints202512.0984.v1

minor penalty in mass and stiffness, while the central diameter *P*3 has the strongest effect, simultaneously decreasing stress and deformation but increasing mass. As a result, the optimum region of the design space is found for combinations with relatively generous blends and fillets and a moderately increased central diameter, which provide a significant reduction in peak stress at almost unchanged total deformation and with only a limited increase in mass.

The response-surface optimisation was carried out in ANSYS Workbench using the MOGA (Multi-Objective Genetic Algorithm) method, with the two objectives defined as **minimise mass P6** and **minimise maximum equivalent stress P7**. The algorithm started from 100 initial samples and, with 100 samples per iteration, converged after 32 evaluations, yielding three non-dominated solutions (Candidate Points 1–3). As summarised in the optimisation Table 3, **Candidate Point 1** corresponds to the geometry with P1=3.3 mm, P2=1.65 mm, P3=13.75 mm, P4=8.1 mm and P5=16.5 mm. This design provides the **lowest maximum equivalent stress** in the spindle region (P7=184.9 MPa), at the cost of a moderate increase in solid mass (P6=0.589 kg) compared with the lighter Candidate Point 2. Given the safety-critical nature of the spindle, the reduction in peak stress is prioritised over the small mass penalty, and Candidate Point 1 is therefore selected as the **optimal spindle geometry** for further assessment.

Table 3. Optimization results for the wheel spindle geometry: design parameters and objective functions for the three candidate solutions.

Parameter	Unit	Candidate Point 1	Candidate Point 2	Candidate Point 3
P1 - Blend1.FD1	mm	3.30	3.30	2.70
P2 - R14	mm	1.65	1.65	1.65
P3 - V10	mm	13.75	11.25	13.75
P4 - V8	mm	8.10	8.10	8.10
P5 - V9	mm	16.50	13.50	16.50
P6 - Solid mass	kg	0.5887	0.4935	0.5895
P7 - Eq. stress max.	MPa	184.92	265.38	187.72

The von Mises stress field for the optimised spindle geometry (Candidate Point 1) is shown in Figure 20. The global maximum of about 220 MPa occurs at the edge of a bolt hole in the mounting flange, whereas the stresses in the safety-critical transition between the flange and the spindle shaft are reduced to approximately 180–185 MPa. Compared with the baseline design, this corresponds to a clear reduction of the peak stress in the spindle fillet while keeping the overall stress level in the surrounding flange at a similar magnitude, confirming the effectiveness of the geometric changes identified by the optimisation.

Preprints.org (www.preprints.org) | NOT PEER-REVIEWED | Posted: 19 December 2025 doi:10.20944/preprints202512.0984.v1

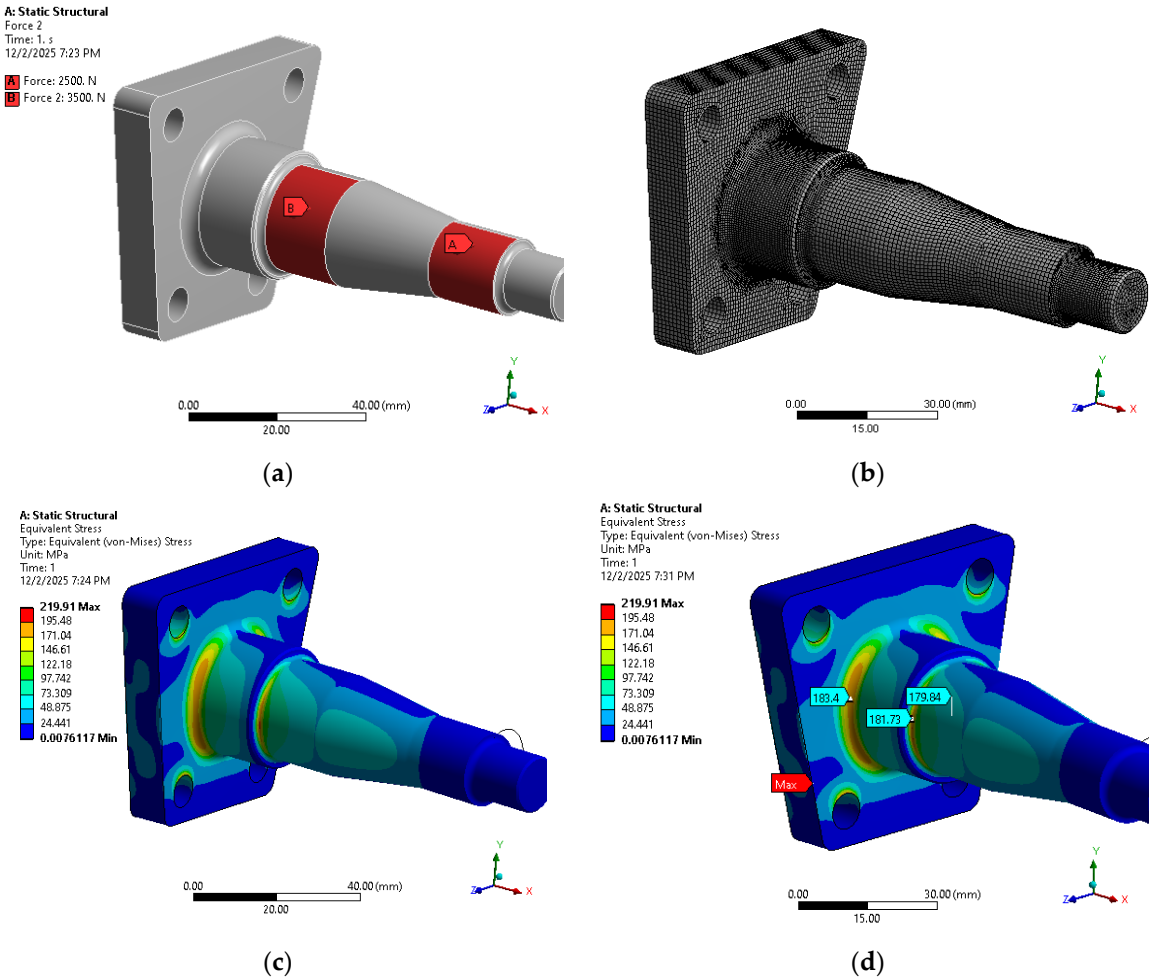

Figure 20. Static structural analysis of the optimised wheel spindle under the maximum admissible wheel load: (**a**) loading configuration with forces of 2500 N and 3500 N applied on the two bearing seats; (**b**) finite element mesh of the spindle and mounting flange; (**c**) global equivalent von Mises stress distribution; (**d**) detailed view of the transition region between the flange and spindle, showing stress levels around 180–185 MPa in the fillet.

The spindle analysis was carried out under the maximum admissible wheel load transmitted through the two bearing seats, as illustrated in Figure 20, a. The load is applied as two concentrated forces acting on the cylindrical regions corresponding to the inner rings of the bearings (A and B), with magnitudes of 2500 N and 3500 N, respectively, consistent with the bearing manufacturer's load ratings for the considered axle. All stress results presented for the baseline and optimised spindle therefore refer to this worst-case bearing load combination. The highest stresses in the spindle fillet are around 180–185 MPa, significantly lower than in the baseline design.

7. Discussion

The results obtained from the combined multibody, experimental and FE analyses provide a coherent picture of the structural behaviour of the rear axle under durability loading and highlight several aspects that are directly relevant for design optimisation.

First, the flexible multibody model of the test bench and rear axle proved to be an effective tool for defining realistic boundary conditions for the structural analysis. By tuning the kinematic excitation so that the translational and rotational amplitudes of the axle and stabilizer bar match those observed in service, the reaction forces at the wheel spindles and in the key joints of the mechanism could be determined in a manner consistent with the actual stiffness of the suspension assembly. This is an important difference compared with purely static approaches in which arbitrary loads are applied to the axle, and it explains why the equivalent design load used in the FE model is

 doi:10.20944/preprints202512.0984.v1

significantly lower than typical peak service loads: it represents the reaction corresponding to the prescribed displacement imposed by the fatigue test bench, not the absolute worst-case wheel load.

The experimental strain measurements confirm that the stand reproduces a highly repeatable cyclic loading condition, with stable amplitudes and phases over many cycles. The good agreement between measured and simulated stresses—differences of about 10% at the beam mid-span and comparable magnitudes at the other instrumented points—indicates that the FE model successfully captures both the global stiffness of the axle and the local stress distribution in the regions of interest. This level of correlation is satisfactory for design purposes and justifies the use of the FE model to extrapolate the stress field to locations that are not instrumented experimentally and to perform parametric modifications that would be difficult or expensive to test directly.

The FE stress maps show that the most critical areas are not located in the mid-span of the axle beam, where the stresses are moderate and well distributed, but rather in the junction regions between the beam, side arms and spindle brackets. This observation is consistent with classical fatigue design principles, which identify geometric discontinuities and load-path changes as typical origins of crack initiation. In particular, the corner at the base of the spindle stands out as a clear hot spot. The fact that this region is also the most safety-critical from a functional point of view (loss of the wheel in case of fracture) motivates the decision to focus the optimisation effort on the wheel spindle geometry.

The response-surface-based optimisation provides additional insight into the sensitivity of the spindle behaviour to changes in key geometric parameters. The response surfaces for deformation, stress and mass show that the central diameter and the transition geometry (blend length and fillet radius) play distinct roles: increasing these dimensions tends to reduce the maximum equivalent stress and deformation, at the expense of a moderate increase in mass. Within the practical bounds dictated by bearing fits and packaging, the algorithm identifies an optimum region with generous blends and a slightly larger central diameter, where the peak stress is substantially reduced while the increase in mass and the change in stiffness remain limited. Candidate Point 1, selected as the optimal design, embodies this compromise and demonstrates how small, targeted geometric changes can significantly improve fatigue strength without redesigning the entire axle.

Several limitations of the present study should also be acknowledged. The analysis focuses on a single, predominantly vertical loading case representative of a specific durability test; other loading scenarios (e.g., combined vertical and lateral loads, braking or cornering events) have not yet been considered. Material behaviour has been assumed linear elastic, and the fatigue assessment is currently based on stress levels rather than a full life prediction using S–N or ε–N curves. The models of rubber bushings and joints are simplified, and weld geometries are idealised, which may influence local stress peaks. These aspects point towards natural extensions of the work, including multi-load-case optimisation, more detailed modelling of joints and weld toes, and integration of fatigue-life criteria directly into the optimisation loop.

Despite these limitations, the study demonstrates that integrating a validated test bench, flexible multibody simulation, FE analysis and response-surface optimisation forms a powerful framework for the design and refinement of safety-critical suspension components. The methodology is generic and can be transferred to other axle types, front-suspension links or even to different vehicle classes, facilitating systematic improvements in durability with a controlled impact on weight and cost.

8. Conclusions

This work presented an integrated numerical–experimental methodology for the durability assessment of a passenger-car rear axle, combining a dedicated test bench, flexible multibody simulation in MSC ADAMS and explicit dynamic finite element analysis in ANSYS.

The main outcomes can be summarised as follows:

- A rear suspension durability test bench was designed and built to reproduce, in a controlled and repeatable manner, the cyclic loading acting on a dependent rear axle. The kinematic layout of the rocker mechanism and the symmetric excitation of the wheel-spindle regions were chosen

 doi:10.20944/preprints202512.0984.v1

such that the translational and rotational amplitudes of the axle and stabilizer bar are representative of real operating conditions.

- A detailed flexible multibody model of the bench–axle system was developed in ADAMS, including deformable representations of the rear axle and stabilizer bar. The simulations provided time histories of displacements, deformations and joint reaction forces, and allowed the equivalent design load applied at the wheel spindles to be defined in a way consistent with the actual stiffness of the suspension assembly.
- An experimental strain analysis was carried out on the rear axle mounted on the test bench, using nine strain-gauge locations strategically placed along the beam, heads and trailing arms. The recorded stresses in the stabilised regime showed excellent repeatability over successive cycles and confirmed the predominantly bending–torsion loading mode.
- An explicit dynamic FE model of the rear axle was built in ANSYS, with boundary conditions mirroring the stand configuration and loads taken from the multibody simulation. The von Mises stress field highlighted a critical region in the corner where the bent side plate joins the side arm (peak stress ≈ 104 MPa), as well as moderate but relevant stresses in the beam mid-span and in the beam heads.
- A quantitative correlation between FE predictions and experimental stresses at the strain-gauge locations showed differences within about 10% at the beam mid-span and similar orders of magnitude at the other points. The model thus reproduces both the absolute stress levels and the relative distribution along the axle, correctly identifying the same fatigue-critical areas as the measurements.

Overall, the results demonstrate that the combined use of a dedicated test bench, flexible multibody simulation and explicit dynamic FE analysis provides a robust and consistent framework for the structural assessment and optimisation of rear axle assemblies. The methodology can be extended to alternative axle geometries, different suspension layouts and more complex loading histories, and forms a solid basis for future work on design optimisation and fatigue life prediction under representative service conditions.

Author Contributions: Conceptualization, I.D.G. and I.D.; methodology, I.D.G. and I.D.; software, I.D.G.; validation, L.R. and C.C.; formal analysis, I.D.G.; investigation, I.D.G.; resources, I.D.; data curation, C.C.; writing—original draft preparation, I.D.G.; writing—review and editing, I.D.; visualization, L.R; supervision, I.D.; project administration, I.D.; funding acquisition, I.D. All authors have read and agreed to the published version of the manuscript.

Funding: This research received no external funding.

Conflicts of Interest: The authors declare no conflicts of interest.

References

1. Gobbi, M., Haque, I., Papalambros, P., & Mastinu, G. (2006, September). A critical review of optimization methods for road vehicles design. In 11th AIAA/ISSMO Multidisciplinary Analysis and Optimization Conference (p. 6998).
2. Yıldız, A. R., Özkaya, H., Yıldız, M., Bureerat, S., Yıldız, B. S., & Sait, S. M. (2020). The equilibrium optimization algorithm and the response surface-based metamodel for optimal structural design of vehicle components. Materials Testing, 62(5), 492–496.
3. Kumar, G. S., & Kumaraswamidhas, L. A. (2021). Design optimization focused on failures during developmental testing of the fabricated rear-axle housing. Engineering Failure Analysis, 120, 104999.
4. Zheng, B., Fu, S., & Lei, J. (2022). Topology optimization and multiobjective optimization for drive axle housing of a rear axle drive truck. Materials, 15(15), 5268.

 doi:10.20944/preprints202512.0984.v1

5. Topac, M. M., Karaca, M., Aksoy, B., Deryal, U., & Bilal, L. (2020). Lightweight design of a rear axle connection bracket for a heavy commercial vehicle by using topology optimisation: A case study. Mechanics, 26(1), 64–72.
6. Park, J. H., Kim, S. K., Choi, B. I., Lee, H. J., Lee, Y. H., Kim, J. S., & Kim, K. J. (2010). Optimal design of rear chassis components for lightweight automobile using design of experiment. Materialwissenschaft und Werkstofftechnik, 41(5), 391–397.
7. Topaç, M. M., Tanrıverdi, A., Çolak, O., Bilal, L., & Maviş, M. (2021). Analysis of the failure modes and design improvement of an eccentrically loaded connecting rod for a double front axle steering linkage prototype. Engineering Failure Analysis, 122, 105204.
8. Jeong, T., Lee, S. B., & Yim, H. J. (2017). Shape optimization of a torsion beam axle for improving vehicle handling performance. International Journal of Automotive Technology, 18(5), 813–822.
9. Balta, B., Erk, O., Solak, H. A., & Durakbasa, N. (2014). Pareto optimization of heavy duty truck rear underrun protection design for regulative load cases. SAE International Journal of Commercial Vehicles, 7(2014-01-9027), 726–735.
10. Senniappan, M., More, R., Bhide, S., & Gowda, S. (2016). Optimization of commercial vehicle's steering tie rod arm design based on strain life approach (No. 2016-01-0381). SAE Technical Paper.
11. Zhou, J., Du, Z., Liao, Y., & Tang, A. (2018). An optimization design of vehicle axle system based on multiobjective cooperative optimization algorithm. Journal of the Chinese Institute of Engineers, 41(8), 635–642.
12. Hao, Y. D., He, Z. C., Li, G. Y., Li, E., & Huang, Y. Y. (2018). Uncertainty analysis and optimization of automotive driveline torsional vibration with a driveline and rear axle coupled model. Engineering Optimization, 50(11), 1871–1893.
13. Soares, E. J., De Carvalho, D. M., Onusic, H., Barreiro, J. A., & Ferraro, L. C. (1999). Development of a test bench for static and dynamic tests of a spring leaf for the suspension of commercial vehicles (No. 1999-01-2990). SAE Technical Paper.
14. de Jesus Soares, E., Oliva, A. M., Adas, C. A., Dusi, F. C., Santos, P. S. P., Accurso, M. A. F., & Kliewer, M. (2014). Development of a Multiaxial Bench Test for the Suspension of Commercial Vehicles (No. 2014-36-0019). SAE Technical Paper.
15. Mitra, A. C., Kiranchand, G. R., Soni, T., & Banerjee, N. (2016). Design of experiments for optimization of automotive suspension system using quarter car test rig. Procedia Engineering, 144, 1102–1109.
16. Mitra, A. C., Soni, T., & Kiranchand, G. R. (2016). Optimization of automotive suspension system by design of experiments: a nonderivative method. Advances in Acoustics and Vibration, 2016(1), 3259026.
17. Salah, M. (2017). A Laboratory Automotive Suspension Test Rig: Design, Implementation and Integration. Jordan Journal of Mechanical & Industrial Engineering, 11(2).
18. Alzughaibi, A., Xue, Y., & Grosvenor, R. (2019). A new insight into modelling passive suspension real test rig system with consideration of nonlinear friction forces. Proceedings of the Institution of Mechanical Engineers, Part D: Journal of Automobile Engineering, 233(8), 2257–2266.
19. Siqueira, M. A., Gomes, P. C., Teixeira, E. L. S., Fortaleza, E. L. F., & Morais, M. V. G. (2024). Automation of a Quarter-Car Suspension Test Bench (No. 2024-36-0115). SAE Technical Paper.
20. Liao, Z. C., Bai, X. X. F., Li, Y., Deng, X. C., & Sun, J. (2020). Design, modeling, and verification of a test bench for braking simulation of 1/4 vehicle. Proceedings of the Institution of Mechanical Engineers, Part D: Journal of Automobile Engineering, 234(5), 1425–1441.
21. Croce, P., Orsini, P., & Salvatore, W. (2001). Vibration isolation and design of automotive test benches. Engineering Structures, 23(8), 945–956.
22. Favilli, F., Sgamma, M., Bucchi, F., Frendo, F., Leandri, P., & Losa, M. (2024). A Novel Tire and Road Testing Bench for Modern Automotive Needs. Designs, 8(4), 64.
23. Mántaras, D. A., & Luque, P. (2012). Virtual test rig to improve the design and optimisation process of the vehicle steering and suspension systems. Vehicle System Dynamics, 50(10), 1563–1584.

 doi:10.20944/preprints202512.0984.v1

24. El Hadraoui, H., Zegrari, M., Hammouch, F. E., Guennouni, N., Laayati, O., & Chebak, A. (2022). Design of a customizable test bench of an electric vehicle powertrain for learning purposes using model-based system engineering. Sustainability, 14(17), 10923.
25. Andert, J., Klein, S., Savelsberg, R., Pischinger, S., & Hameyer, K. (2016). Virtual shaft: Synchronized motion control for real time testing of automotive powertrains. Control Engineering Practice, 56, 101–110.